https://doi.org/10.5194/egusphere-2026-4064
Preprint. Discussion started: 11 September 2026

An interpolation-free, natively resolved nest initialization for idealized tropical-cyclone simulations in WRF-ARW v4.5, evaluated against standard nesting and a uniform-mesh reference

Xiuhang Li[1] and Yudi Liu[1]

[1]College of Meteorology and Oceanography, National University of Defense Technology, Changsha, 410073, China

Correspondence: Yudi Liu (udy.liu@pku.edu.cn)

Abstract. Grid nesting is the standard route to convection-resolving resolution in tropical-cyclone (TC) modelling, but in the widely used idealized workflow of the Weather Research and Forecasting model (WRF-ARW) the fine domain is *initialized* by interpolating the coarse parent state onto the fine mesh rather than by sampling the prescribed analytic vortex at the native fine resolution. Because the coarse parent under-resolves the inner core, this interpolated initial vortex carries a broadened radius of maximum wind, weakened radial gradients, and grid-scale truncation imprints, and the first hours of the run are contaminated by a geostrophic-adjustment shock—an inertia–gravity-wave burst and grid-imprinted asymmetries—whose downstream effect on structure and intensity is difficult to control. We present and document a modification to the WRF-ARW (v4.5) idealized nesting initialization that decouples the inner domain from coarse-to-fine interpolation: the source code is altered so that the child domain lays down the prescribed vortex and base-state environment directly at its own $2\,\mathrm{km}$ resolution, sharing the parent's base state and so remaining physically self-consistent. We compare this refined initialization (RE) against the standard official two-domain ($6 \rightarrow 2\,\mathrm{km}$; OR) and three-domain ($18 \rightarrow 6 \rightarrow 2\,\mathrm{km}$; OR_3) configurations, and against a uniform $2\,\mathrm{km}$ single-domain run (UNI) whose inner-core initialization is identical to RE and which therefore serves as a resolution-matched reference solution. With a diagnostic suite—perturbation-vorticity texture and its azimuthal-wavenumber spectrum, time–radius diagrams of diabatic heating, radius–height tangential wind and secondary circulation, low- and upper-level radial profiles, and mean absolute deviation from UNI—we show that OR injects grid-scale pixelated noise and OR_3 a systematic wavenumber-4 truncation artefact, both of which trigger a spurious early adjustment (in OR_3, a transient radius-of-maximum-wind excursion to $\sim 120\,\mathrm{km}$ near $t \approx 8$–$12\,\mathrm{h}$). The refined initialization removes these artefacts, produces a smooth quasi-balanced spin-up with the earliest and deepest boundary-layer inflow and the most compact, upright eyewall, and tracks UNI most closely in every intensity and structure metric (mean absolute deviation of minimum sea-level pressure $0.72\,\mathrm{hPa}$ versus 0.96–$1.08\,\mathrm{hPa}$; near-surface tangential wind $0.35\,\mathrm{m\,s^{-1}}$ versus $\sim 1.7\,\mathrm{m\,s^{-1}}$). Crucially, the compactness of the initial core paces the eyewall life cycle: the boundary-layer inflow, the radius–height eyewall structure, the secondary circulation, and the radius of maximum wind all show RE organizing earliest and the interpolated runs lagging by a consistent offset, so a comparison made at a single lead time can mistake this timing lag for a structural disagreement. The residual RE–UNI difference over the first $36\,\mathrm{h}$ arises not from initialization but from the nesting mechanism itself, and surfaces first—as expected—in the phase

https://doi.org/10.5194/egusphere-2026-4064
Preprint. Discussion started: 11 September 2026

of the most sensitive convective (reflectivity) field. The modification is inexpensive, reproducible, and intended as a reusable improvement and test case for idealized nested TC modelling.

1 Introduction

Limited-area atmospheric models with grid nesting are the standard tool for problems that simultaneously demand a large domain and locally high resolution. The Weather Research and Forecasting model and its Advanced Research dynamical core (WRF-ARW; Skamarock and Klemp, 2008; Skamarock et al., 2019) are among the most widely used community frameworks of this kind. Tropical cyclones (TCs) are a canonical application: the eyewall and rainband dynamics of the inner core demand convection-permitting grid spacing ($\lesssim 3\,\mathrm{km}$), whereas the environmental interaction and outer circulation must be represented across a domain several thousand kilometres wide. Refining the inner-core grid systematically sharpens the eyewall, contracts the radius of maximum wind (RMW), and strengthens the resolved vertical motion (Fierro et al., 2009; Gentry and Lackmann, 2010; Gopalakrishnan et al., 2011), so a high-resolution nest is a prerequisite for credible TC structure. Idealized f-plane experiments initialized with a weak axisymmetric vortex (Rotunno and Emanuel, 1987), as implemented in the WRF `em_tropical_cyclone` test case, are a long-standing workhorse for isolating these inner-core processes from environmental complexity.

In a nested configuration, however, the fine domain does not evolve in isolation. At every fine-grid time step its lateral boundaries are supplied by spatial interpolation from the coarser parent, and lateral boundary conditions are a long-recognized, fundamental limitation of limited-area modelling (Warner et al., 1997). The abrupt change in grid spacing across a nest interface is itself a source of error: features poorly resolved on the coarse grid are spuriously reflected or excited as they cross the interface (Harris and Durran, 2010)—a difficulty common to nesting implementations across modelling systems (e.g., Harris and Lin, 2013; Zängl et al., 2015). In the idealized TC setting this problem is compounded at initialization. The inner domain's initial vortex is generated by interpolating the parent's coarse-grid state onto the fine mesh rather than by sampling the prescribed analytic vortex at the native fine resolution. Because the coarse parent under-resolves the core, the interpolated initial state carries a broadened RMW, weakened radial gradients of potential vorticity and absolute angular momentum, and grid-scale truncation imprints projected onto the fine grid—a vortex that is neither fully resolved nor dynamically self-consistent.

These interpolation artefacts are more than a cosmetic blemish on the initial field. The compactness of the initial core—its RMW, inertial stability, and radial gradients—exerts a first-order control on how efficiently subsequent diabatic heating is converted into intensification (Schubert and Hack, 1982; Vigh and Schubert, 2009), so a smeared initial vortex can bias the spin-up, the organization of the secondary circulation, and the structural evolution from the outset. Moreover, because eyewall contraction and the ensuing eyewall life cycle are themselves paced by the core's compactness and by the strength and depth of the boundary-layer inflow (Stern et al., 2015; Kepert, 2013), a smeared initial vortex does not merely change the *amplitude* of the response: it shifts the *timing* of the whole intensification-and-reorganization sequence, a phasing effect that we find recurs across every time-resolved diagnostic below. Conventional remedies—relaxation/sponge zones, boundary filters, and interior nudging—damp the resulting noise but do not remove the interpolation imprint, and they introduce distortions of

https://doi.org/10.5194/egusphere-2026-4064
Preprint. Discussion started: 11 September 2026

their own within the blending zone (Warner et al., 1997; Harris and Durran, 2010). Crucially, the standard WRF idealized nesting workflow offers no straightforward way to give the inner domain a natively resolved, interpolation-free initial vortex: by construction the fine grid is slaved to the coarse parent both at initialization and at every boundary update.

Here we present a modification to the idealized nesting initialization of WRF-ARW (v4.5) that decouples the inner domain from coarse-to-fine initialization interpolation. Rather than letting the outer domain (`d01`) supply the inner domain (`d02`) with interpolated initial values, we modify the source code so that `d02` is initialized independently, sampling the prescribed vortex and base-state environment directly at its own resolution; because both domains share a single base state, the result is physically self-consistent. This removes the grid-scale, interpolation-induced artefacts at the nest interface and yields a clean, low-wavenumber, dynamically consistent inner-core vortex from $t = 0$. We document the code changes required, contrast the resulting initial and evolving fields with the standard official two-domain (OR) and three-domain (OR_3) configurations, and show that the modified scheme (RE) removes the spurious high-wavenumber signatures present in the interpolated configurations. We further benchmark all three against a uniform $2\,\mathrm{km}$ single-domain integration (UNI) whose inner-core initialization is identical to RE, so that UNI isolates the error contributed by nesting alone. We then assess how the cleaner initialization affects the simulated inner-core structure, secondary circulation, and intensification of the TC, paying particular attention to how the initial-core compactness paces the timing of eyewall contraction and secondary-circulation reorganization across the four runs.

The remainder of the paper is organized as follows. Section 2 describes the WRF-ARW configuration, the idealized balanced vortex, the four experiments (RE, OR, OR_3 and UNI) and the diagnostic suite. Section 3 documents the initial-state interpolation artefact and its removal by the native modification; Sect. 4 follows the artefact into the convective and structural evolution; and Sect. 5 evaluates intensity, the deviation from the UNI benchmark, and the residual nesting error. Sections 6–7 summarize the findings and discuss their implications for idealized nested modelling. The model version, modified source code, and namelists needed to reproduce the experiments are archived as detailed in the code and data availability section.

2 Model configuration and experiment design

2.1 WRF-ARW set-up and nested-domain geometry

The experiments use the Advanced Research dynamical core of the Weather Research and Forecasting model (WRF-ARW v4.5; Skamarock and Klemp, 2008; Klemp et al., 2007; Skamarock et al., 2019), a fully compressible, nonhydrostatic solver that integrates the Euler equations on a terrain-following mass coordinate with a split-explicit, time-split scheme, in its idealized `em_tropical_cyclone` configuration. The set-up is idealized: an f-plane with constant Coriolis parameter $f = 5.0\times10^{-5}\,\mathrm{s}^{-1}$ (representative of $\sim$20° latitude), a horizontally homogeneous environment, no background flow, and a fixed sea-surface temperature. The baseline nested configuration uses two horizontal domains: the parent (`d01`) has grid spacing $\Delta x = 6\,\mathrm{km}$ and the child (`d02`) has $\Delta x = 2\,\mathrm{km}$, an odd refinement ratio of 3 so that each parent cell maps onto a 3×3 block of child cells (Fig. 1). An odd ratio places child cell centres symmetrically about parent cell centres, which simplifies the interpolation stencil and avoids a systematic half-cell offset of the vortex centre. A three-domain variant adds a still-coarser outer parent ($18\to6\to2\,\mathrm{km}$, ratio 3 at each interface), so that the innermost $2\,\mathrm{km}$ domain is reached through two successive coarse-

https://doi.org/10.5194/egusphere-2026-4064
Preprint. Discussion started: 11 September 2026

to-fine interpolations; this defines the OR_3 configuration of Sect. 2.4. In both configurations the outermost parent domain spans $3240 \times 3240\,\mathrm{km}$ (540×540 cells at $6\,\mathrm{km}$ in the two-domain configuration; 180×180 cells at $18\,\mathrm{km}$ in the three-domain configuration), and the innermost $2\,\mathrm{km}$ domain spans $720 \times 720\,\mathrm{km}$ (360×360 cells) in both configurations, with an additional intermediate $6\,\mathrm{km}$ domain spanning $2160 \times 2160\,\mathrm{km}$ (360×360 cells) in the three-domain configuration; all domains are centred on the vortex, so that the storm core remains far from any lateral boundary over the analysis period. All domains share the same vertical grid—51 vertically stretched levels from the surface to a model top at $\sim 25\,\mathrm{km}$, with an upper-level Rayleigh damping layer in the top $5\,\mathrm{km}$ to absorb vertically propagating gravity waves—and, apart from one exception noted below, the same physics. The $6\,\mathrm{km}$ and $2\,\mathrm{km}$ time steps are $30\,\mathrm{s}$ and $10\,\mathrm{s}$ respectively in every configuration ($30\,\mathrm{s}$ for the $6\,\mathrm{km}$ parent domain of the two-domain configuration, or $90\,\mathrm{s}$ for the $18\,\mathrm{km}$ outer parent of the three-domain configuration, each scaled successively by the refinement ratio of 3); acoustic substepping follows the split-explicit default. Nesting uses the standard WRF two-way feedback (`feedback=1`, with feedback smoothing `smooth_option=1`): the child is forced at its lateral boundaries by the time-evolving parent and in turn feeds its interior back onto the overlapping parent cells at every step. Convective-scale motions are treated explicitly on every $6\,\mathrm{km}$ and $2\,\mathrm{km}$ domain in both configurations (no cumulus parameterization; `cu_physics=0`), with the Thompson bulk microphysics scheme (`mp_physics=8`; Thompson et al., 2008), a Mellor–Yamada–Janjic (MYJ) planetary-boundary-layer scheme (`bl_pbl_physics=2`; Janjić, 1994), and the paired Eta-similarity surface-layer scheme (`sf_sfclay_physics=2`; Janjić, 1994) to compute surface enthalpy and momentum fluxes[1]. The only physics difference between the two configurations is that the additional, coarser $18\,\mathrm{km}$ domain of the three-domain configuration uses parameterized convection (`cu_physics=6`, Tiedtke scheme), consistent with the WRF recommendation that cumulus parameterization is generally needed at grid spacings $\geq 10\,\mathrm{km}$; the nesting treatment is otherwise the only difference between experiments.

2.2 Idealized balanced vortex

The initial vortex follows the sectionally continuous parametric wind profile of Willoughby et al. (2006), which reproduces observed hurricane radial structure more faithfully than single-exponential or Rankine forms and, like other complete-structure parametric models (Chavas et al., 2015), represents both the inner-core and the outer wind field. The axisymmetric tangential wind increases as a power of radius inside the eye,

$$V(r) = V_{\max}\left(\frac{r}{R_{\max}}\right)^{n}, \qquad r \leq R_{\max}, \tag{1}$$

where the exponent n (here $n \approx 1$) controls the steepness of the inner wind rise, and decays as a weighted sum of two exponentials outside it,

$$V(r) = V_{\max}\left[(1-A)\,e^{-(r-R_{\max})/X_1} + A\,e^{-(r-R_{\max})/X_2}\right], \qquad r \geq R_{\max}, \tag{2}$$

with a smooth polynomial ramp joining the two branches across a transition zone $R_1 \leq r \leq R_2$ spanning the RMW (Willoughby et al., 2006). We use $V_{\max} = 20\,\mathrm{m\,s^{-1}}$, $R_{\max} = 40\,\mathrm{km}$, transition radii $R_1 = 23.1\,\mathrm{km}$ and $R_2 = 48.1\,\mathrm{km}$, dual decay lengths

[1]The namelist also sets `isftcflx=1`, which modifies the surface enthalpy/momentum exchange coefficients at high wind speeds; per the WRF User's Guide this option is documented for use with `sf_sfclay_physics=1`, so its behaviour under `sf_sfclay_physics=2` should be verified against the compiled code before being relied upon.

https://doi.org/10.5194/egusphere-2026-4064
Preprint. Discussion started: 11 September 2026

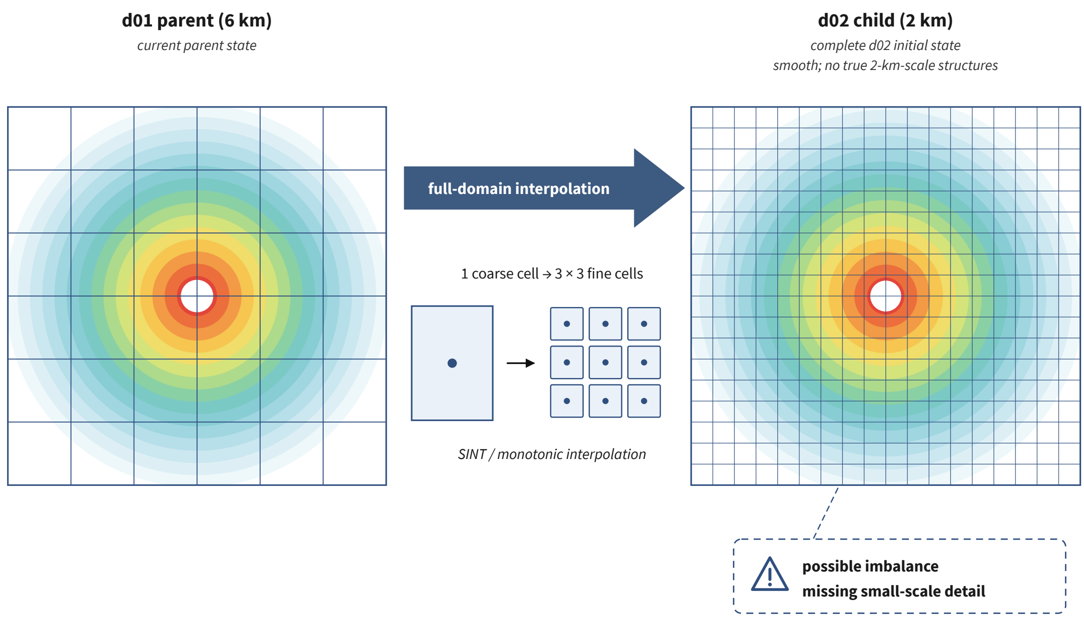

Figure 1. Schematic of nest activation (Step 1, initialization). The 6 km parent (d01) is interpolated over the whole child footprint to create the 2 km child (d02) initial state, with each coarse cell mapped onto a 3×3 block; the interpolated inner core is smooth but may be imbalanced and carries grid-scale truncation imprints. The complementary operation—the continuous coarse-to-fine boundary forcing that acts throughout the integration—is shown later alongside its downstream signature in Fig. 15.

X_1 and X_2 with outer weight A, and a smooth taper to zero wind beyond $r_{\text{taper}} = 600\,\text{km}$ to avoid a discontinuity at the domain scale (Fig. 2a). The corresponding axisymmetric relative vorticity,

$$\zeta(r) = \frac{1}{r}\frac{\mathrm{d}[rV(r)]}{\mathrm{d}r}, \tag{3}$$

peaks at $\zeta_{\max} = 14.1 \times 10^{-4}\,\text{s}^{-1}$ near $r = 31.8\,\text{km}$, just inside the RMW, and remains everywhere well above the planetary vorticity f in the core (Fig. 2b), so the vortex is inertially stiff and balance-dominated. The three-dimensional mass and thermodynamic fields are obtained by iteratively enforcing gradient-wind and hydrostatic balance with the prescribed wind, following the analytic construction of Reed and Jablonowski (2011) (see also the companion idealized test case of Reed and Jablonowski, 2012); this same balanced state is the common target for all experiments. In the vertical, the tangential wind retains its full amplitude through the lower and middle troposphere and is tapered smoothly to zero between roughly 12 km and the tropopause, so that the vortex is warm-cored and the primary circulation is confined below the outflow layer; the two-dimensional horizontal structure discussed throughout refers to the lower-tropospheric levels ($z \lesssim 2\,\text{km}$) unless otherwise stated.

https://doi.org/10.5194/egusphere-2026-4064
Preprint. Discussion started: 11 September 2026

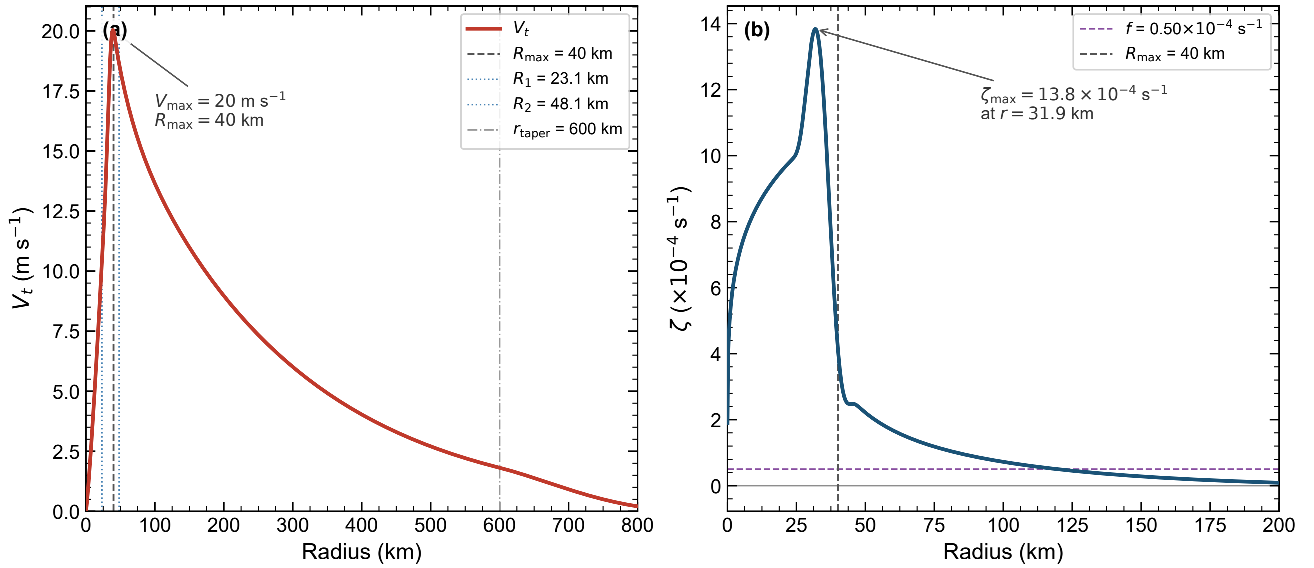

Figure 2. Idealized initial vortex. (a) Axisymmetric tangential wind $V(r)$ from the Willoughby et al. (2006) profile, Eqs. (1)–(2), with $V_{\max} = 20\,\mathrm{m\,s^{-1}}$ at $R_{\max} = 40\,\mathrm{km}$, transition radii $R_1 = 23.1\,\mathrm{km}$, $R_2 = 48.1\,\mathrm{km}$, and taper radius $r_{\mathrm{taper}} = 600\,\mathrm{km}$. (b) Corresponding relative vorticity $\zeta(r)$, Eq. (3), peaking at $14.1 \times 10^{-4}\,\mathrm{s^{-1}}$ near $r = 31.8\,\mathrm{km}$; the planetary vorticity $f = 0.5 \times 10^{-4}\,\mathrm{s^{-1}}$ is shown for reference.

2.3 Reference run and nesting strategies

The reference simulation, UNI, discretizes the entire inner-domain footprint at $\Delta x = 2\,\mathrm{km}$ in a single domain and is integrated from $t = 0$ with the analytic vortex of Sect. 2.2 sampled directly at $2\,\mathrm{km}$. Crucially, its inner-core initialization is *identical* to that of the refined scheme RE (Sect. 2.4): both lay down the same natively resolved, interpolation-free vortex, so RE and UNI share the same initial state to machine precision. Because UNI contains no coarse parent, no interpolation step, and no internal lateral boundary, it is by construction free of nest-initialization and coupling error at $2\,\mathrm{km}$ resolution. This is not a claim of physical "truth"—UNI shares the model's parameterization uncertainty—but it is the correct *numerical* reference for the question posed here: how much does a nested $2\,\mathrm{km}$ solution differ from the $2\,\mathrm{km}$ solution it is trying to approximate, purely because of nesting? Since RE and UNI start identical, any RE–UNI difference that develops must come from the nesting mechanism (boundary coupling and two-way feedback) rather than from initialization—a decomposition we exploit in Sect. 5. All nesting skill in Sect. 3 is measured relative to UNI.

2.4 The four experiments

Four integrations are compared. All target the same analytic vortex; they differ only in how the $2\,\mathrm{km}$ inner-core initial state is produced.

https://doi.org/10.5194/egusphere-2026-4064
Preprint. Discussion started: 11 September 2026

RE (refined, independent initialization; recommended). The two-domain ($6 \to 2\,\mathrm{km}$) configuration with the code modification of Sect. 3.2: the $2\,\mathrm{km}$ inner domain is initialized natively, sampling the analytic vortex directly with no coarse-to-fine interpolation. Its initial inner core is therefore identical to UNI.

OR (official two-domain nesting). The standard, unmodified two-domain ($6 \to 2\,\mathrm{km}$) configuration: the $2\,\mathrm{km}$ inner state is produced by one coarse-to-fine interpolation of the $6\,\mathrm{km}$ parent, as in Sect. 3.1. It carries the grid-scale pixelated interpolation noise inherent to remapping an under-resolved coarse vortex onto a fine mesh.

OR$_3$ (official three-domain nesting). The standard, unmodified three-domain ($18 \to 6 \to 2\,\mathrm{km}$) configuration; the subscript 3 denotes the three domains. The $2\,\mathrm{km}$ inner state is now produced by *two* successive coarse-to-fine interpolations, so truncation error accumulates and the interpolation imprint is both stronger and more systematic than in OR, taking the form of a geometric wavenumber-4 artefact aligned with the square mesh (Sect. 3.3).

UNI (uniform-mesh reference). The single-domain $2\,\mathrm{km}$ run of Sect. 2.3, initialized identically to RE but with no nest at all; it isolates the error contributed by nesting itself.

Compactly, writing ϕ^c for the $2\,\mathrm{km}$ inner-core initial state, ϕ^a for the analytic vortex sampled natively at $2\,\mathrm{km}$, $I_{k\to k+1}$ for one coarse-to-fine interpolation, and ϕ^{18}, ϕ^6 for the 18 and $6\,\mathrm{km}$ parent states,

$$\text{RE, UNI:} \quad \phi^c = \phi^a, \tag{4}$$

$$\text{OR:} \quad \phi^c = I_{6\to 2}[\phi^6], \tag{5}$$

$$\text{OR}_3\text{:} \quad \phi^c = I_{6\to 2}\big[I_{18\to 6}[\phi^{18}]\big]. \tag{6}$$

Because the analytic vortex fixes the axisymmetric primary circulation, all four runs begin from essentially the same azimuthal-mean tangential-wind profile (Sect. 4.2); they diverge only in the two-dimensional texture and balance of the interpolated cases. This is the central design feature: the storm is held fixed and only the nest-initialization numerics vary. We note that the specific wavenumber-4 imprint of OR$_3$ (Sect. 3.3) reflects the interaction of the square-mesh interpolation stencil with the inner-core geometry; the qualitative result—that repeated coarse-to-fine interpolation injects a systematic, geometrically organised truncation artefact—is general, but the dominant wavenumber itself is configuration-dependent, and we do not claim otherwise.

2.5 Diagnostic suite

The strategies are ranked with a compact, reproducible diagnostic suite chosen to expose imbalance at initialization and to trace its downstream consequences.

1. *Initial-state imbalance.* The azimuthally averaged radial wind $V_r(r)$ at $t = 0$ measures departure from balance directly: a perfectly balanced axisymmetric vortex has $V_r \equiv 0$, so any finite V_r at initialization is spurious. More precisely, V_r here measures departure from the *discrete gradient-wind* state on the child mesh—the state the model itself treats as balanced—

https://doi.org/10.5194/egusphere-2026-4064
Preprint. Discussion started: 11 September 2026

rather than from a continuous analytic balance, so that grid-scale interpolation residual and any genuine (but here absent by design) forced overturning are cleanly separated (Sect. 3.3).

2. *Azimuthal-wavenumber decomposition.* The perturbation vorticity $\zeta'(r,\lambda) = \zeta - \overline{\zeta}(r)$ is expanded in azimuthal Fourier modes at each radius; we report the amplitude $A_n(t)$ of wavenumbers $n = 1$–6 obtained as the Fourier coefficient magnitude averaged over the inner-core annulus ($r = 20$–$80\,\mathrm{km}$) at $z = 1\,\mathrm{km}$ and normalised by the axisymmetric ($n = 0$) vorticity, which tracks the growth of spurious asymmetries and their organisation into structures that resemble vortex-Rossby-wave (VRW) activity (Montgomery and Kallenbach, 1997; McWilliams et al., 2003). We describe these as VRW-*like* because their low-wavenumber, inner-core character is consistent with VRW dynamics; a full phase-propagation attribution is beyond the present scope (Sect. 3.4).

3. *Convective organization.* Time–radius (Hovmöller) diagrams of the diabatic heating rate at several altitudes, and their pairwise differences, reveal whether initialization artefacts perturb the eyewall and rainband heating (Sect. 4.1).

4. *Structural evolution.* Radius–height sections of tangential wind, the transverse (secondary) circulation—vertical velocity, a mass streamfunction, and absolute angular momentum—and radial profiles at low and upper levels characterize the balanced response and, read across their full time axis, expose the RE-leading timing lag in eyewall contraction and secondary-circulation reorganization (Sect. 4.2).

5. *Deviation from the benchmark.* For each intensity metric m we report the mean absolute deviation from UNI over the first $36\,\mathrm{h}$,

$$\overline{|\Delta m|} = \frac{1}{T}\int_0^T \left| m_X(t) - m_{\mathsf{UNI}}(t) \right| \mathrm{d}t, \qquad T = 36\,\mathrm{h}, \tag{7}$$

where $X \in \{\mathsf{RE}, \mathsf{OR}, \mathsf{OR}_3\}$ (Sect. 5). The $36\,\mathrm{h}$ window isolates the adjustment phase, during which nesting artefacts are most influential and least confounded by later nonlinear divergence.

6. *Precipitation validation.* Simulated radar reflectivity is compared between the best nesting strategy and UNI as an integrated check on convective realism (Sect. 5.1).

3 The interpolation artefact and its removal

3.1 Standard interpolated initialization

In the standard WRF idealized nesting workflow the fine domain is not given its own analytic vortex; instead its entire initial state is generated by interpolating the already-initialized coarse parent onto the refined mesh (Fig. 1). The default routine distributes each coarse-grid value over its 3×3 block of fine cells with a monotone, shape-preserving interpolation that is high-order where the field is smooth but reverts toward linear near sharp gradients to suppress overshoots (Skamarock et al., 2019). This produces a complete fine-grid initial field, but it *cannot* manufacture genuine $2\,\mathrm{km}$-scale structure that is absent from the

https://doi.org/10.5194/egusphere-2026-4064
Preprint. Discussion started: 11 September 2026

$6\,\mathrm{km}$ parent: the interpolated inner core is broadened, its radial gradients are weakened, and the remapping projects grid-scale truncation error onto the fine mesh. Thereafter (Step 2, Fig. 15) the fine domain is advanced with its lateral boundaries forced by the time-evolving parent through a narrow specified/relaxation zone of the Davies type (Davies, 1976), and—because WRF nesting is two-way by default—its interior is fed back onto the overlapping parent cells at every step. The initial interpolation imprint and the ongoing coarse-to-fine boundary forcing are the two mechanisms this study targets.

3.2 Native-resolution modification

The modification is confined to the initialization stage. Rather than letting the fine domain inherit the interpolated parent state, we alter the idealized-case initialization in the WRF-ARW source so that the fine domain constructs the prescribed analytic vortex (Sect. 2.2) and base-state environment *directly on its own* $2\,\mathrm{km}$ *grid*, exactly as a single-domain idealized run would. Parent and child share one base state, so the two-domain system remains physically self-consistent, and the coarse-to-fine boundary forcing of Step 2 is left unchanged. The change therefore isolates the effect of the initial interpolation: the fine core is natively resolved and interpolation-free from $t = 0$, while everything downstream of initialization is identical to the standard run. In practice the modification touches only the routine that populates the nest's initial arrays and requires no change to the solver, the boundary code, or the namelist physics; the exact source edits and namelists are provided in the code and data availability section.

3.3 Initial-state imbalance and texture

At $t = 0$ the four runs share, to plotting accuracy, the same azimuthal-mean tangential-wind profile at both low ($z = 1\,\mathrm{km}$) and upper ($z = 15\,\mathrm{km}$) levels (Figs. 3a and 4a), confirming that the primary circulation is fixed by the common analytic target. The azimuthally averaged radial wind at $t = 0$, by contrast, is the direct measure of imbalance (diagnostic 1 of Sect. 2.5): RE has $V_r \equiv 0$ to plotting accuracy, whereas OR and OR_3 already carry a finite spurious V_r—of order $10^{-4}\,\mathrm{m\,s^{-1}}$ at low level (Fig. 3e) and an order of magnitude smaller aloft ($10^{-5}\,\mathrm{m\,s^{-1}}$; Fig. 4e). These amplitudes are tiny, but because they are unbalanced they are the seed of the adjustment burst analysed in Sect. 3.4; that the imbalance is ten times larger at $z = 1\,\mathrm{km}$ than at $z = 15\,\mathrm{km}$ already localizes the artefact to the lower-tropospheric core, where the analytic vortex has its sharpest radial gradients and the coarse-to-fine remapping distorts them most. The remaining (non-$t = 0$) panels of Figs. 3–4 record the downstream *timing* of the spin-up and are analysed together with the vertical structure in Sect. 4.2; here we stay at $t = 0$ and turn to the two-dimensional texture. That texture at $z = 2\,\mathrm{km}$ differs markedly among the runs (Fig. 5a–c). The refined, natively initialized vortex (RE) shows an almost circular high-vorticity annulus surrounding a smooth inner core. The radial gradient across the annulus is sharp but spatially continuous, and the wind vectors remain organized around a common centre; there is no visible point-scale or mesh-aligned noise. This is the expected texture of a vortex that has been sampled directly on the $2\,\mathrm{km}$ grid and is therefore dynamically self-consistent on that mesh.

The official two-domain run (OR) has the same mean vortex, but its annulus is already corrugated at $t = 0$. The high-vorticity ring is broken into alternating enhanced and weakened patches, giving the field a pixelated, grid-scale texture with short spatial correlation length. This is not a resolved physical asymmetry of the analytic vortex; it is the imprint left when the

https://doi.org/10.5194/egusphere-2026-4064
Preprint. Discussion started: 11 September 2026

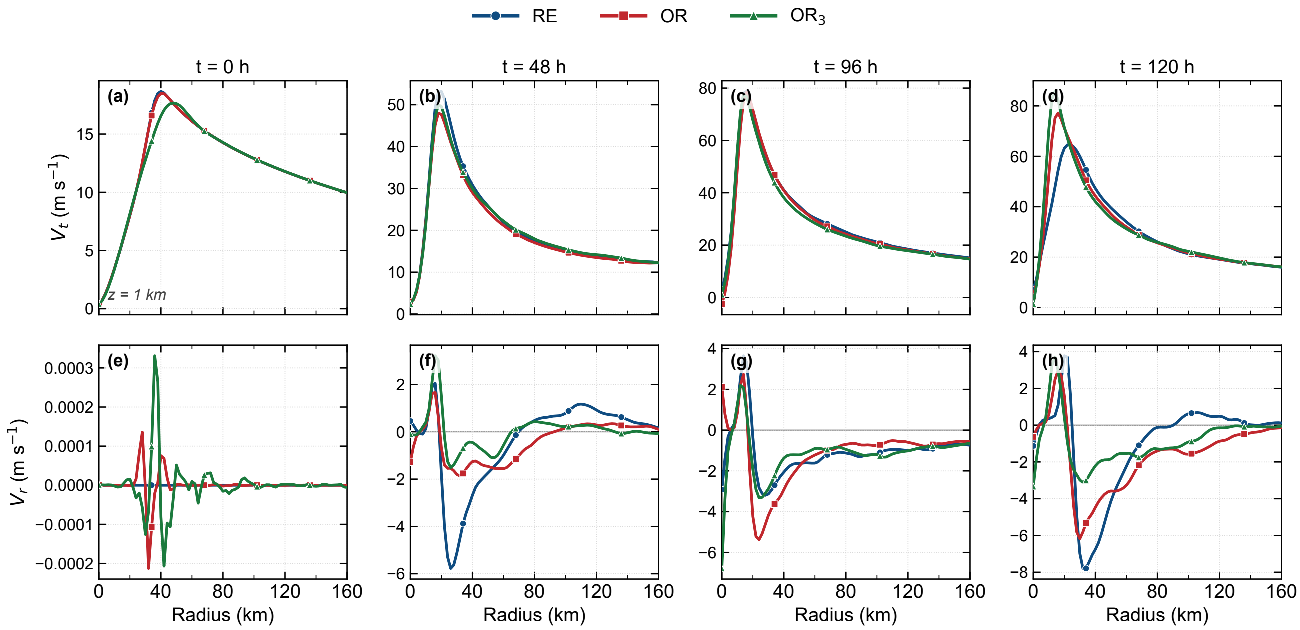

Figure 3. Radial profiles at $z = 1\,\mathrm{km}$ of (a–d) tangential wind V_t and (e–h) radial wind V_r at $t = 0$, 48, 96 and 120 h for RE, OR and OR_3. At $t = 0$ (panel e) the raw strategies show finite spurious V_r of order $10^{-4}\,\mathrm{m\,s^{-1}}$, whereas RE is balanced.

under-resolved $6\,\mathrm{km}$ parent vortex is interpolated onto the $2\,\mathrm{km}$ child grid. The three-domain case (OR_3) shows an even more systematic imprint: its vorticity field is locally smoother than the noisy OR mosaic, but the annulus is visibly distorted into a square-grid, fourfold pattern, and the outer edge is polygonal rather than circular—evidence that the repeated $18 \to 6 \to 2\,\mathrm{km}$ interpolation has projected truncation error onto the inner-core geometry in an organized way.

By $t = 4\,\mathrm{h}$ all three vortices have begun the barotropic breakdown and axisymmetrization of the initially thin, high-vorticity annulus (Fig. 5d–f), as expected for hurricane-like annular vorticity rings (Melander et al., 1987; Schubert et al., 1999; Kossin and Schubert, 2001). What differs is the texture carried into this breakdown. In RE the annulus rolls up from a clean initial ring into small-scale filaments and mesovortex-like structures around the eyewall, but the disruption stays tied to the vortex's own annular instability. In OR the breakdown proceeds on top of the pre-existing pixelated perturbations, so the eyewall contains a noisier sequence of compact vorticity maxima and minima. In OR_3 the early evolution retains a more organized, azimuthally asymmetric character, with broader spiral-like filaments and a less circular outer edge. Figure 5 thus shows that the interpolated runs do not merely differ at the initial instant: the interpolation texture is rapidly incorporated into the first few hours of vortex breakdown and sets the asymmetry field analysed spectrally in Sect. 3.4.

https://doi.org/10.5194/egusphere-2026-4064
Preprint. Discussion started: 11 September 2026

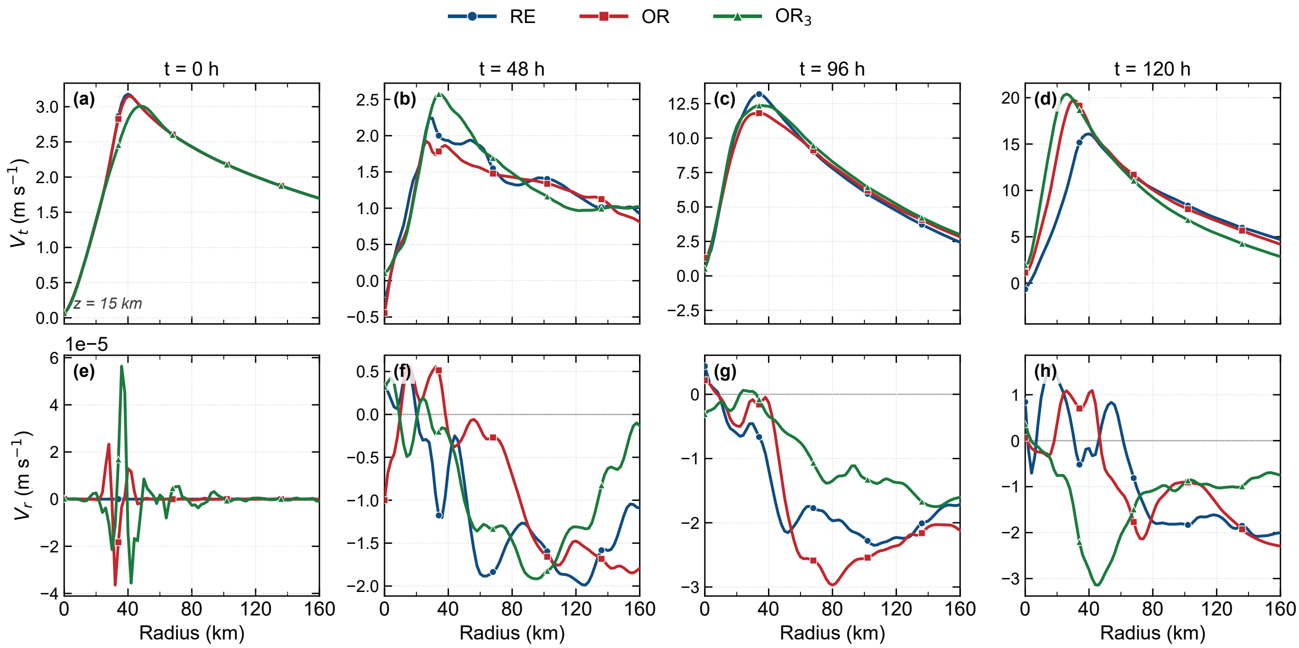

Figure 4. As Fig. 3 but at $z = 15\,\mathrm{km}$. The $t = 0$ imbalance in the raw strategies is of order $10^{-5}\,\mathrm{m\,s^{-1}}$ (panel e); RE remains balanced.

3.4 Growth of spurious asymmetries

Because the interpolation-induced imbalance is not axisymmetric, it projects onto discrete azimuthal wavenumbers. Figure 6 shows the full perturbation vorticity at $t = 0$ together with the time evolution of the wavenumber amplitudes A_n ($n = 1$–6) and selected individual modes. The initial fields already reveal a clear separation among the three strategies. In RE, the initial ζ' field is weak, smooth and dominated by a low-wavenumber structure, with a broad quasi-crescent anomaly around the inner core and no point-scale noise. This indicates that the natively initialized child vortex is dynamically coherent on the $2\,\mathrm{km}$ mesh. In OR, by contrast, the full ζ' field is fragmented into alternating positive and negative patches with a pixelated texture, consistent with coarse-grid truncation error being projected onto the fine mesh during the $6\,\mathrm{km}$–$2\,\mathrm{km}$ interpolation. In $\mathrm{OR_3}$, the initial perturbation is not random but organized into a regular wavenumber-4 pattern aligned with the square grid. This geometric symmetry suggests an interpolation-stencil artefact rather than a freely selected vortex mode; the two successive interpolations in the three-domain configuration make this imprint more systematic than in OR.

The amplitude time series show how these initial imprints adjust. In RE the low wavenumbers evolve smoothly: the dominant modes amplify gradually and then weaken as the vortex axisymmetrizes, while the higher wavenumbers stay small. In OR the first several hours are instead marked by rapid oscillations across multiple modes, especially $n = 1$–4, the signature of an unbalanced-adjustment episode in which the interpolated vortex radiates inertia–gravity waves while recovering the fine-grid balance. The $\mathrm{OR_3}$ spectrum carries the clearest imprint of the imposed geometry: the early wavenumber-4 component is

https://doi.org/10.5194/egusphere-2026-4064
Preprint. Discussion started: 11 September 2026

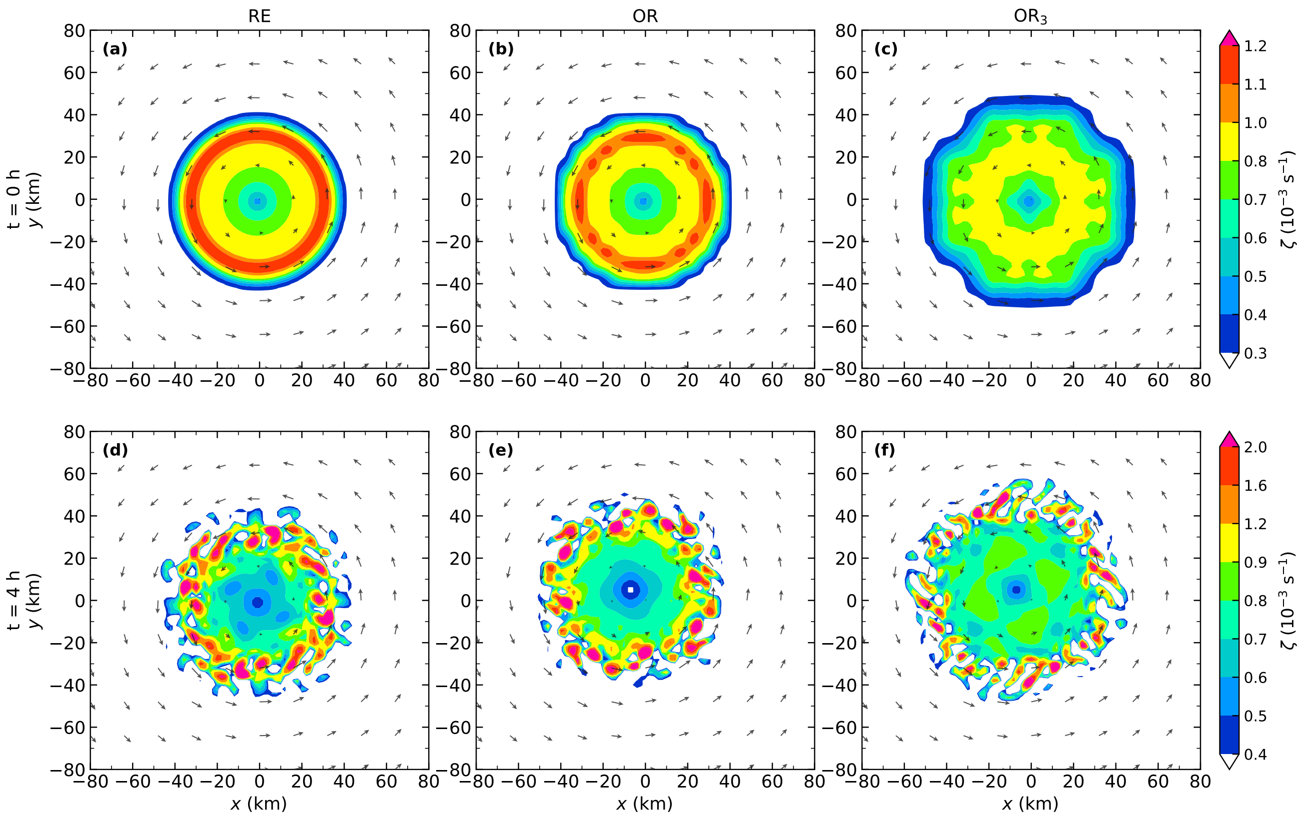

Figure 5. Relative vorticity (shading, $10^{-3}\,s^{-1}$) and horizontal wind vectors for RE, OR and OR_3 at (a–c) $t = 0$ h and (d–f) $t = 4$ h. All panels share a common colour scale so the strategies are directly comparable. At $t = 0$ the three strategies share the same primary circulation but differ in two-dimensional texture; by $t = 4$ h all have begun the barotropic breakdown of the high-vorticity annulus.

strong, and several modes oscillate nearly synchronously around $t \approx 8$–12 h—the same period as the transient RMW excursion discussed in Sect. 5. This timing links the three-domain RMW jump to the adjustment of the interpolation-induced asymmetry field, although we do not attempt a formal wave–mean-flow attribution here.

The individual-mode maps and the full vorticity–wind fields show how these spectral differences enter the early vortex evolution. By $t = 4$ h RE develops a coherent spiral-like low-wavenumber anomaly, consistent with vortex-Rossby-wave-like deformation on the radial vorticity gradient (Montgomery and Kallenbach, 1997; Reasor et al., 2004). In OR and OR_3, by contrast, strong wavenumber-4 anomalies remain concentrated near the eyewall and extend outward in wrapped filaments. The corresponding full fields (Fig. 5d–f) confirm that all three vortices have begun the barotropic breakdown and axisymmetrization characteristic of a thin, high-vorticity annulus (Melander et al., 1987; Schubert et al., 1999; Kossin and Schubert, 2001). The key difference is that RE enters this stage from a relatively clean, low-wavenumber perturbation, whereas OR and OR_3 carry into the breakdown an asymmetry spectrum inherited from their interpolated initialization: the early filamentation and

https://doi.org/10.5194/egusphere-2026-4064
Preprint. Discussion started: 11 September 2026

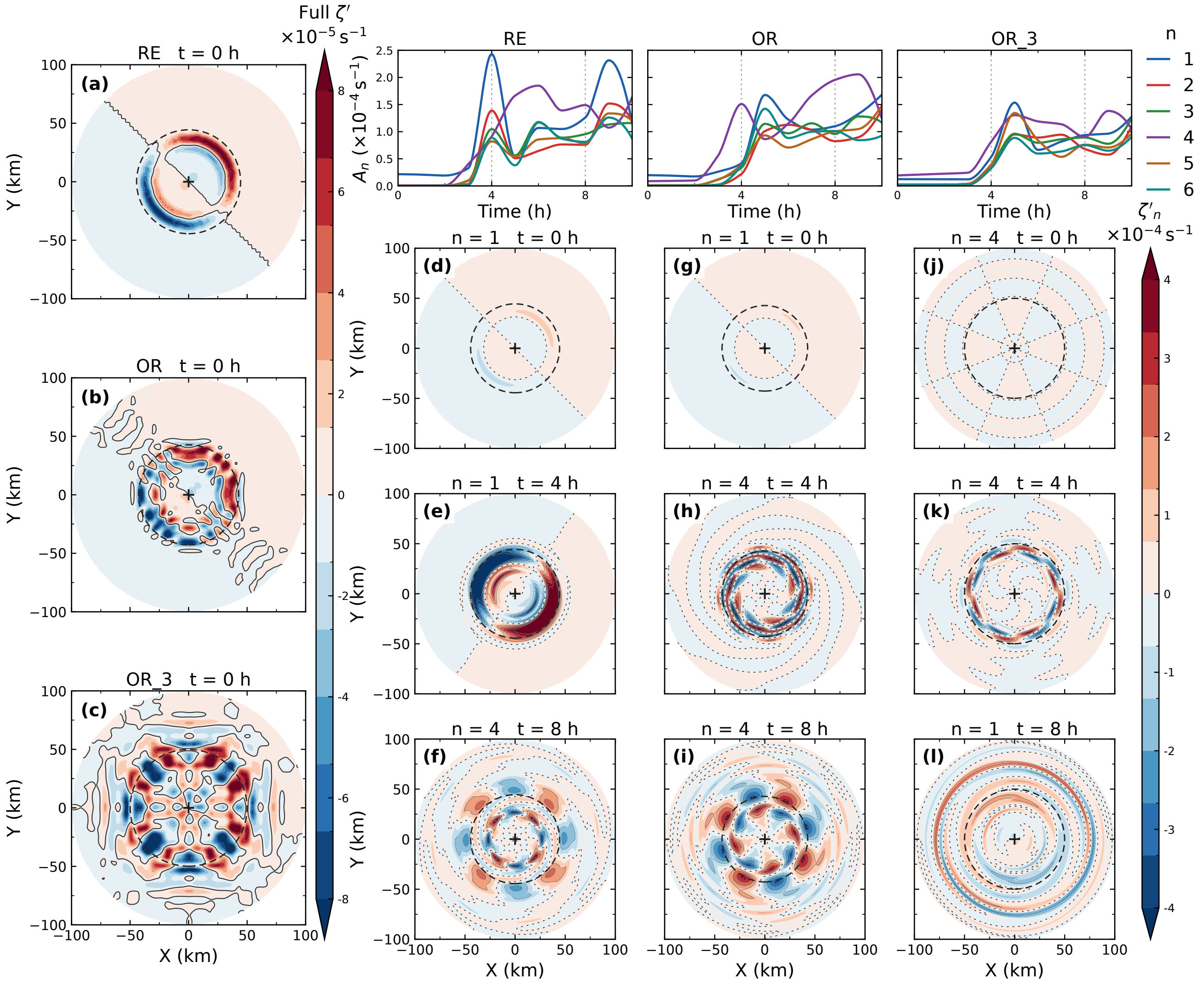

Figure 6. Azimuthal-wavenumber analysis of perturbation vorticity ζ'. Left column: full ζ' at $t = 0$ h for RE, OR and OR$_3$. Upper right: time series of the amplitudes A_n of wavenumbers $n = 1$–6, computed as the Fourier-coefficient magnitude of ζ' averaged over the $r = 20$–80 km annulus at $z = 1$ km and normalised by the axisymmetric ($n = 0$) vorticity. Remaining panels: selected individual modes at $t = 0$, 4 and 8 h. The refined initialization produces smooth low-wavenumber deformation, whereas the official interpolated strategies seed grid-controlled asymmetries, including pixelated multiscale noise in OR and a coherent wavenumber-4 artefact in OR$_3$.

https://doi.org/10.5194/egusphere-2026-4064
Preprint. Discussion started: 11 September 2026

rearrangement in the official runs are not purely the storm's own dynamical response but are already contaminated by grid-controlled perturbations.

By $t = 8\,\mathrm{h}$ the RE perturbation has weakened and spread into thinner filaments, consistent with continuing axisymmetrization. The interpolated runs retain larger residual asymmetries, OR preserving stronger wavenumber-4 remnants and OR_3 shifting toward a broader low-wavenumber distortion during its early recovery. In short, OR and OR_3 do not merely start noisier; they impose a specific, grid-controlled asymmetry field that the vortex subsequently advects, shears, and partly axisymmetrizes.

4 Downstream response: convection and structure

4.1 Convective organization

The initialization signature reaches the diabatic heating. Time–radius diagrams of the heating rate at 3.2, 6.0 and $9.6\,\mathrm{km}$ (Fig. 7) show the same qualitative eyewall–rainband life cycle in all three configurations—a continuous deep-red eyewall heating band near $r \approx 20$–$40\,\mathrm{km}$ flanked by outward-sloping rainband streaks—but they differ in early temporal coherence. In RE the eyewall heating is temporally continuous from $t = 0$ and the outward-propagating rainband streaks are smooth and quasi-periodic, so the run enters productive convective evolution immediately. In OR and OR_3 the eyewall heating and rainband streaks are broken and discontinuous during the first $\sim 24\,\mathrm{h}$—the thermodynamic counterpart of the adjustment shock, as the model radiates spurious energy before organized latent heating can settle. We use "geostrophic adjustment" here in its finite-Rossby-number sense: the inertially stiff core (Sect. 2.2) is in gradient-wind rather than geostrophic balance, so the unbalanced initial increment relaxes toward the discrete gradient-wind state while shedding inertia–gravity waves. A second, robust difference is a shallow suppression (weak-cooling) ring just outside the eyewall whose extent increases as $\mathrm{RE} < \mathrm{OR} < \mathrm{OR}_3$, with OR_3 showing both the broadest suppression and the strongest, widest inner-core heating.

The pairwise differences (Fig. 8) sharpen the comparison. Their dominant signal is a radially adjacent red–blue *dipole* straddling the eyewall radius rather than a single-signed offset—the fingerprint of an eyewall sitting at a slightly different radius in each configuration, so that the difference is positive at one run's eyewall and negative at the other's. The dipole is weak and broken early and saturates into a deep vertical couplet by $t \approx 48\,\mathrm{h}$, showing that the eyewall-position difference grows with the integration. It is deepest for $\mathrm{RE} - \mathrm{OR}_3$ and remains clear even for $\mathrm{OR} - \mathrm{OR}_3$, so the two official (interpolated) configurations also differ systematically in eyewall placement. Outside the core the differences are low-amplitude and speckled, so the sensitivity to nest initialization is concentrated at the eyewall. Hovmöller diagrams localize *where* the heating differs but cannot by themselves establish the mechanism; the inner-core-excitation interpretation is corroborated by the secondary-circulation diagnostics below.

4.2 Structural evolution: core compactness and the eyewall life-cycle lag

The initial-core differences documented in Sects. 3.3–3.4 do not merely decay: they fix the compactness of the developing vortex and, through it, the *timing* of the eyewall life cycle. We read this timing in three linked views—the radius–height

https://doi.org/10.5194/egusphere-2026-4064
Preprint. Discussion started: 11 September 2026

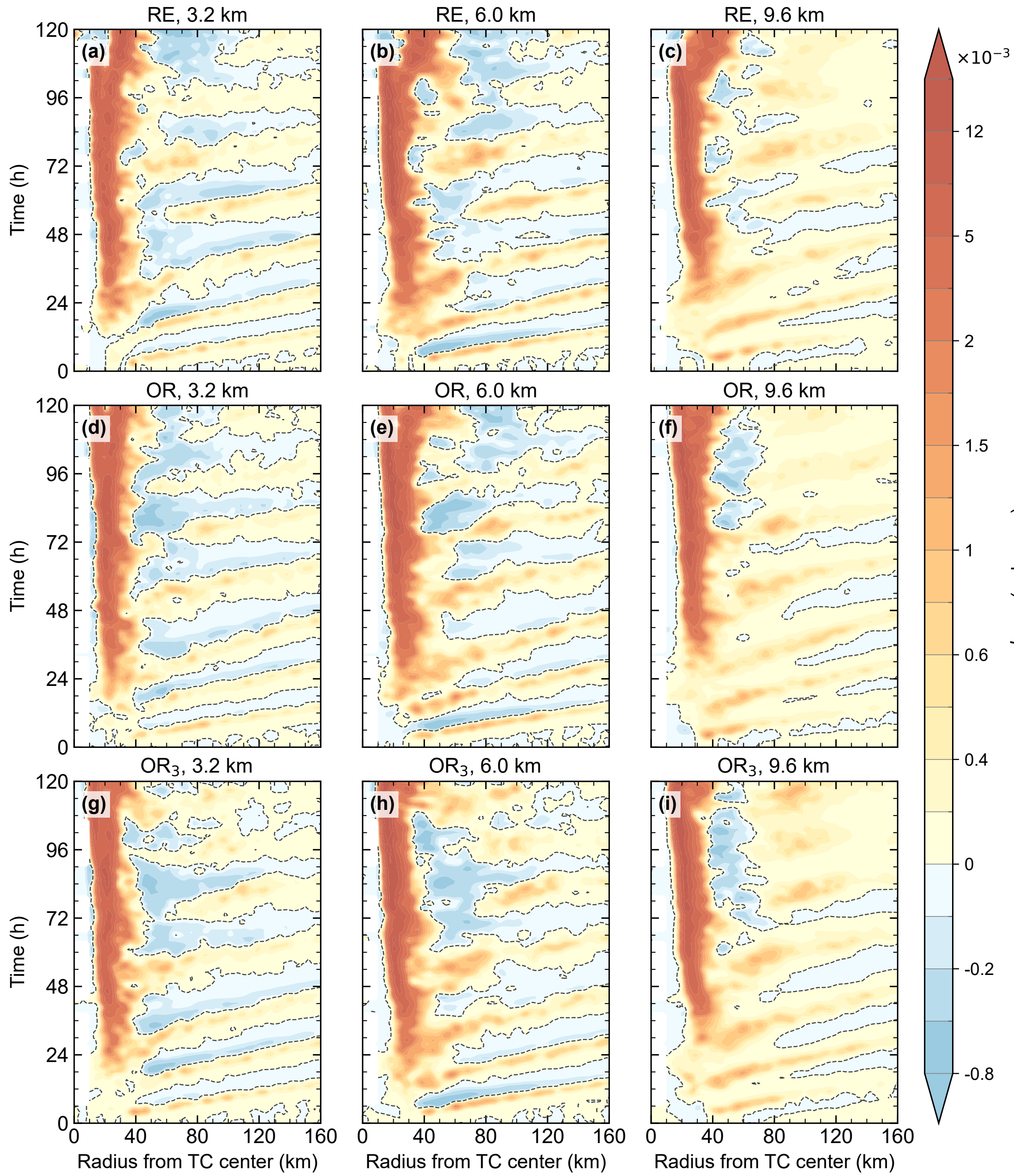

Figure 7. Time–radius (Hovmöller) diagrams of the diabatic heating rate at 3.2, 6.0 and 9.6 km (columns) for RE, OR and OR_3 (rows), showing the contracting eyewall heating and episodic outer maxima.

https://doi.org/10.5194/egusphere-2026-4064
Preprint. Discussion started: 11 September 2026

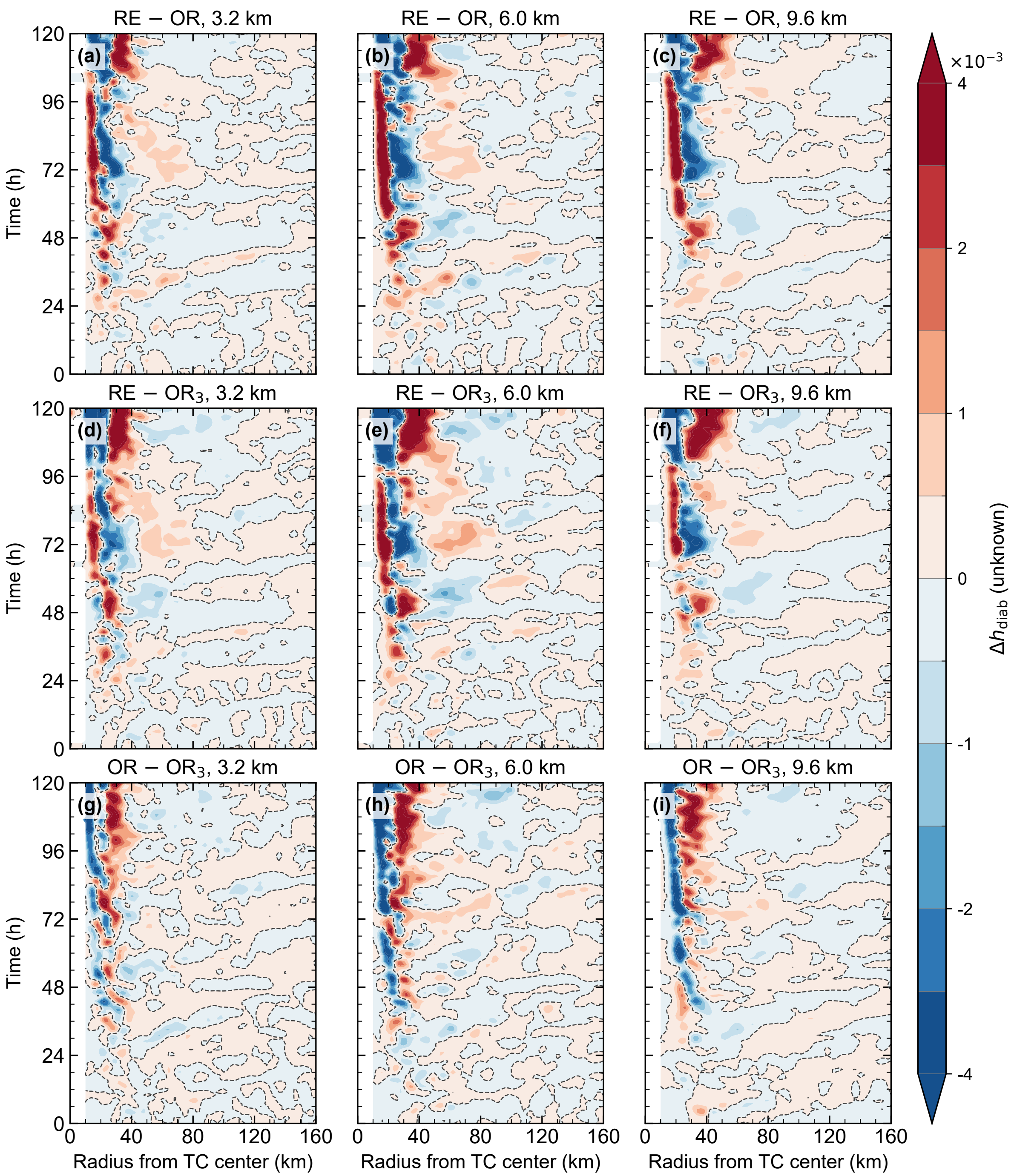

Figure 8. Pairwise differences of the diabatic-heating Hovmöller diagrams of Fig. 7 (RE – OR, RE – OR$_3$, OR – OR$_3$; rows) at the three altitudes (columns). Differences are largest in the developing-eyewall annulus during the first two days and decay as the storm matures.

https://doi.org/10.5194/egusphere-2026-4064
Preprint. Discussion started: 11 September 2026

tangential wind (Fig. 9), the low- and upper-level radial profiles over the whole run (Figs. 3–4), and the secondary circulation (Fig. 10)—because the same ordering, RE leading and OR_3 trailing, appears in all three.

Radius–height tangential wind. As the vortices intensify (Fig. 9), the RMW slope $\mathrm{RMW}(z)$ tilts strongly outward with height early on and progressively becomes near-vertical as the eyewall contracts, with the wind maximum near the top of the boundary layer, consistent with the classical picture of eyewall contraction and upright-eyewall development (Stern and Nolan, 2009; Stern et al., 2015). All three configurations and UNI develop a recognizable, intensifying TC with a warm-core-consistent decay of V_t toward the tropopause, so none of the initializations is pathological. Read column by column, however, the panels expose a systematic lag. At $t = 24\,\mathrm{h}$ (Fig. 9a,f,k) RE already carries a more contracted, less outward-tilted RMW than OR, whereas OR_3 still shows a transient upper-level artefact left by its adjustment shock (Sect. 5). Through $t = 48$–$72\,\mathrm{h}$ RE holds the tightest, most upright eyewall and the steepest outer-core V_t gradient; OR lags slightly in low-level contraction; and OR_3 remains broadest. The separation is easy to underestimate because the mature panels look superficially alike, but by $t = 120\,\mathrm{h}$ the *azimuthal-mean* structure has diverged again markedly (Fig. 9e,j,o): RE still holds a compact, upright eyewall with the RMW pinned near the boundary-layer top, whereas OR_3 has a broader, more diffuse wind field whose $17\,\mathrm{m\,s^{-1}}$ isotach reaches farther outward—a more radially dispersed absolute-angular-momentum distribution (Smith et al., 2009)—with OR intermediate. The same $120\,\mathrm{h}$ separation is visible in the low-level azimuthal-mean profile (Fig. 3d), where the RE tangential-wind peak is sharper and sits at smaller radius than the broader, outward-displaced OR_3 peak. The $t = 0$ compactness ordering of Sect. 3.3 is thus not erased by the spin-up; it re-emerges in the mature azimuthal-mean wind field.

Low- and upper-level radial profiles over the run. The radial figures whose $t = 0$ panels established the initial imbalance (Sect. 3.3) also record the timing of the spin-up when read across their later columns. At low level (Fig. 3) the tangential-wind panels (b–d) show RE reaching a stronger, more sharply peaked core earliest: it already leads at $t = 48\,\mathrm{h}$ (b), the peak magnitudes partly converge by $t = 96\,\mathrm{h}$ (c), and the $t = 120\,\mathrm{h}$ profile (d) separates again, mirroring Fig. 9. The radial-wind panels (f–h) make the mechanism explicit. At $t = 48\,\mathrm{h}$ (f) RE has by far the deepest, most inward boundary-layer inflow (minimum $\approx -5.8\,\mathrm{m\,s^{-1}}$ near $r \approx 28\,\mathrm{km}$, versus $\approx -2\,\mathrm{m\,s^{-1}}$ for OR and OR_3), so it converges absolute angular momentum inward and organizes the eyewall earliest (Kepert, 2001; Smith et al., 2009); the inflow strengths largely converge by $t = 96\,\mathrm{h}$ (g), and by $t = 120\,\mathrm{h}$ (h) the profiles differ once more in the radius and depth of the inflow—the low-level fingerprint of the different eyewall-reorganization stages the runs have reached. The upper level (Fig. 4) tells the same story one layer up: the $t = 0$ imbalance there is an order of magnitude smaller than at low level (panel e, $\sim 10^{-5}\,\mathrm{m\,s^{-1}}$ versus $\sim 10^{-4}\,\mathrm{m\,s^{-1}}$ in Fig. 3e), confirming that the interpolation artefact is concentrated in the lower-tropospheric core, while the later panels (b–d, f–h) show the outflow-layer tangential wind and its radial (outflow) branch strengthening earliest and most coherently in RE—the upper-level counterpart of the low-level inflow lead.

Secondary circulation and the eyewall life-cycle lag. The transverse circulation ties the low- and upper-level timing together and highlights the dynamical pathway most directly (Fig. 10). During the mature stage all three runs develop the canonical in–up–and–out overturning circulation: boundary-layer inflow rises in the eyewall, the mass streamfunction (ψ) cell closes around this rising branch, and the absolute-angular-momentum (M) surfaces are drawn inward and upward through the eyewall, consistent with the balanced vortex response to diabatic heating (Eliassen, 1951; Shapiro and Willoughby, 1982; Emanuel,

https://doi.org/10.5194/egusphere-2026-4064
Preprint. Discussion started: 11 September 2026

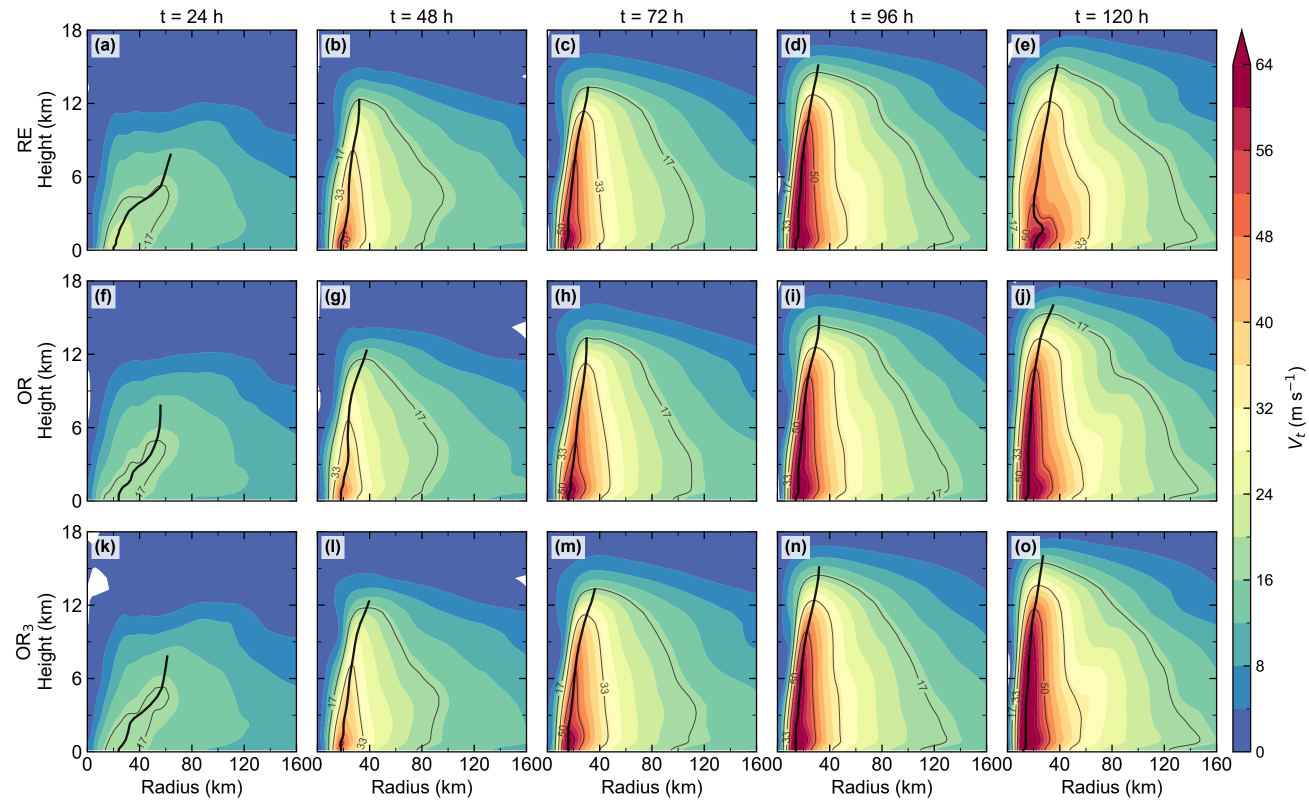

Figure 9. Radius–height sections of tangential wind for RE, OR and OR$_3$ (rows) at $t = 24$, 48, 72, 96 and 120 h (columns). The thick line marks the RMW slope. RE contracts to a compact, upright eyewall earliest; note that by $t = 120$ h (rightmost column) the azimuthal-mean structures have re-diverged, OR$_3$ carrying the broadest, most outward-reaching wind field.

1986). The differences are in the compactness, tilt and—centrally here—the timing of this overturning. In RE (Fig. 10a–e) the eyewall updraught is narrow, deep and nearly upright, with tightly packed M surfaces and a contracted, closed ψ cell, the signature of the strongest primary–secondary coupling and of a vertically compact core. In OR (Fig. 10f–j) the ascent remains strong but the cell is broader, and a mid-level subsidence moat develops just outside the eyewall from about $t \gtrsim 96$ h, signalling an outer-core reorganization and a tendency toward concentric (secondary-eyewall) structure (Willoughby et al., 1982; Sitkowski et al., 2011; Rozoff et al., 2012; Abarca and Montgomery, 2013). In OR$_3$ (Fig. 10k–o) the rising branch is broadest and most outward-sloping, the M surfaces are least contracted, and the ψ cell is most diffuse. Read as a sequence rather than as three static states, these panels describe a single life cycle sampled at different phases: because a more compact, inertially stiffer core converts eyewall heating into spin-up more efficiently (Schubert and Hack, 1982; Hack and Schubert, 1986; Vigh and Schubert, 2009), RE contracts and builds its upright, tightly coupled updraught earliest, while OR and OR$_3$ reach the same compact configuration progressively later. The compactness ordering also shapes the *outer* core: the moat and concentric tendency appear most clearly in OR, whose broader mature wind field is the more favourable to secondary-eyewall

https://doi.org/10.5194/egusphere-2026-4064
Preprint. Discussion started: 11 September 2026

organization (Rozoff et al., 2012; Abarca and Montgomery, 2013), whereas the tightly held RE core expands least and shows the weakest outer reorganization within 120 h. Either way the pathway is common, and it is the boundary-layer inflow that clocks it: the run with the earliest, deepest inflow (Fig. 3f) is the run whose eyewall updraught organizes and replaces first (Kepert, 2001, 2013). This phase lag is not a separate effect but the downstream expression of the single initial-core difference imposed at $t = 0$; Sect. 5 shows that the RMW and intensity records register it too.

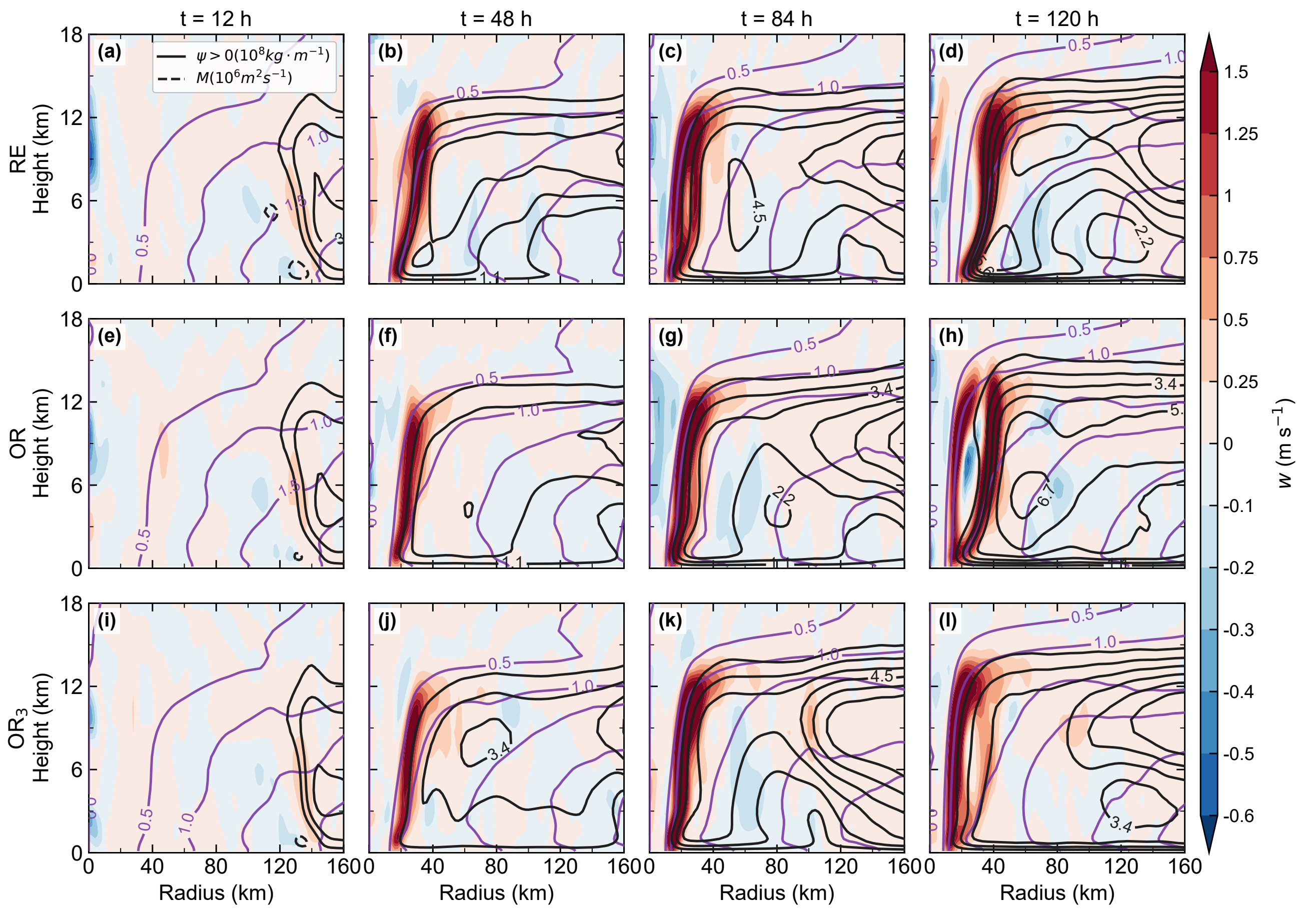

Figure 10. Secondary (transverse) circulation at $t = 72$–120 h for RE, OR and OR_3 (rows): vertical velocity (shading), mass streamfunction (black contours) and absolute angular momentum (purple contours).

5 Intensity, benchmark deviation, and residual nesting error

Over the full 120 h all three configurations deepen into intense cyclones with broadly similar minimum-pressure and peak-wind time series (Fig. 11a), so at the level of headline intensity the choice of nest initialization is second-order. The RMW and peak-1 km-wind curves, however, project the structural lag of Sect. 4.2 into intensity space (Fig. 11b). RE deepens almost

https://doi.org/10.5194/egusphere-2026-4064
Preprint. Discussion started: 11 September 2026

monotonically from $t = 0$ with a smoothly contracting RMW—the same early, efficient organization seen in its compact radius–height structure (Fig. 9) and tightly coupled secondary circulation (Fig. 10). OR_3 instead undergoes a violent early transient: its RMW jumps to $\sim 120\,\mathrm{km}$ near $t \approx 8$–$12\,\mathrm{h}$ before contracting back within a day—a gradient-wind-adjustment shock in which the three-domain interpolated boundary state, inconsistent with the fine core, forces large-amplitude inertia–gravity waves whose adjustment transiently inflates the outer tangential wind and hence the diagnosed RMW. OR shows a weaker version of the same early adjustment. Beyond the shock, the peak-wind (dashed) curves carry the same ordering more quietly: RE builds its $1\,\mathrm{km}$ tangential-wind maximum earliest, consistent with its earliest deep inflow (Fig. 3f). The configurations largely converge in peak intensity after $t \approx 96\,\mathrm{h}$, but the small residual spread late in the run is not noise: it is the intensity image of the runs occupying different phases of one contraction-and-reorganization life cycle (Fig. 10), with OR_3 retaining a systematic offset consistent with the continued injection of asymmetry by its two-step interpolated boundaries and with its broader, more slowly organizing core.

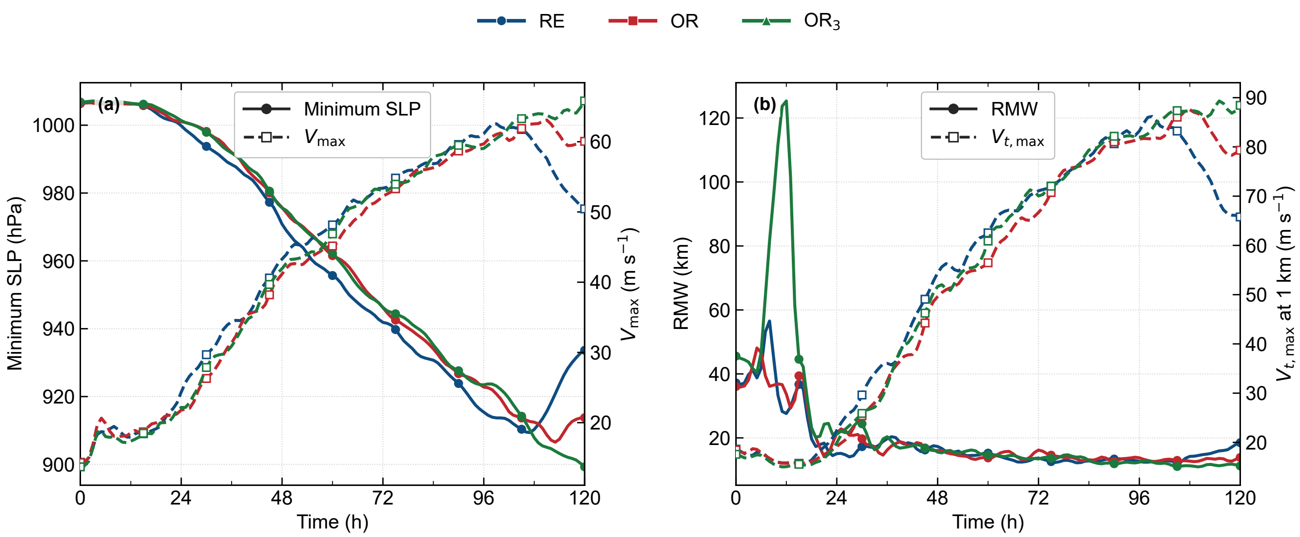

Figure 11. Intensity evolution over $120\,\mathrm{h}$ for RE, OR and OR_3. (a) Minimum sea-level pressure (solid) and maximum $10\,\mathrm{m}$ wind (dashed). (b) Radius of maximum wind (solid) and peak $1\,\mathrm{km}$ tangential wind (dashed).

The benchmark comparison separates nesting error from everything else. Because RE and UNI start from an identical inner core (Sect. 2.3) and their early reflectivity is essentially the same (Sect. 5.1), any RE–UNI divergence is attributable to the nesting mechanism itself—the fine domain's boundaries being supplied each step by the coarser parent, and the two-way feedback approximation—rather than to initialization. Figure 12 compares UNI, RE, OR and OR_3 over the first $36\,\mathrm{h}$ for minimum sea-level pressure, maximum $10\,\mathrm{m}$ wind, peak $1\,\mathrm{km}$ tangential wind, and peak low-level inflow; RE shades most closely around the UNI curve, while OR and especially OR_3 show larger early transients.

Table 1 quantifies this with the mean absolute deviation from UNI of Eq. (7). RE is closest to the benchmark in every metric, and by a wide margin in the kinematic fields: its near-surface tangential-wind deviation ($0.35\,\mathrm{m\,s^{-1}}$) is about one-fifth that

https://doi.org/10.5194/egusphere-2026-4064
Preprint. Discussion started: 11 September 2026

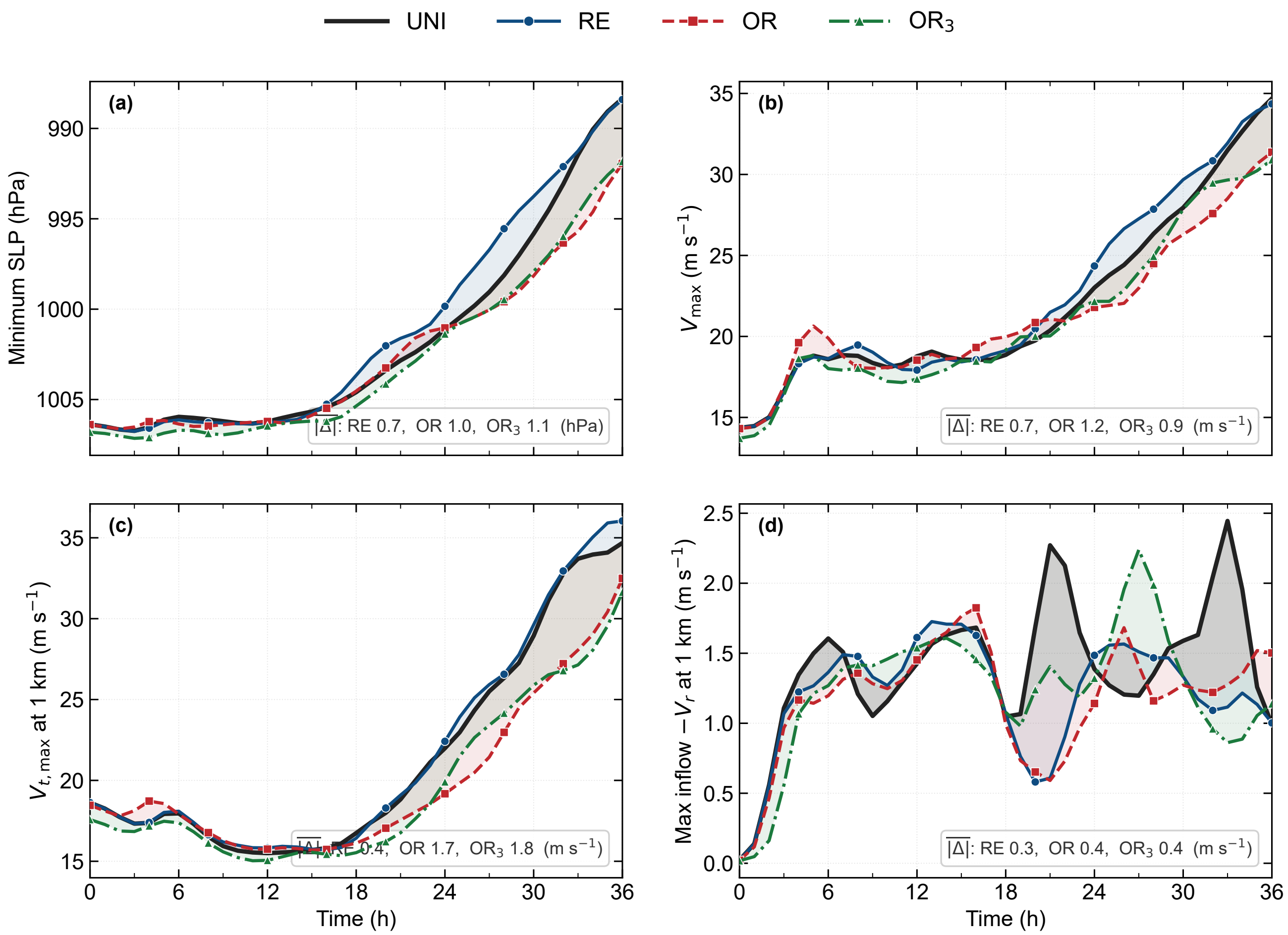

Figure 12. First 36 h evolution of UNI (benchmark), RE, OR and OR$_3$: (a) minimum sea-level pressure, (b) maximum 10 m wind, (c) peak 1 km tangential wind, and (d) peak low-level inflow. In-panel labels give the mean absolute deviation from UNI, Eq. (7). RE tracks UNI most closely.

of the interpolated configurations (1.73 and $1.78\,\mathrm{m\,s^{-1}}$), and its minimum-pressure deviation ($0.72\,\mathrm{hPa}$) is the smallest of the three—a sub-hPa, sub-$\mathrm{m\,s^{-1}}$ level that approaches the model's hour-to-hour jitter, the appropriate standard given that RE and UNI share an initial state. The distributional view of Fig. 13 tells the same story: the RE distributions of minimum pressure, peak 1 km tangential wind, and RMW overlap the UNI distributions most fully, whereas OR$_3$ carries a long tail of large RMW values—the fingerprint of its early adjustment shock and broadened interpolated core.

Two caveats bound the strength of these numbers. First, the deviations in Table 1 come from single realisations, so the smallest gaps—notably the peak low-level inflow (0.32 vs 0.36 vs $0.38\,\mathrm{m\,s^{-1}}$)—are the least robust; we therefore rest the ranking on the fields where the separation is large (near-surface tangential wind, minimum pressure) rather than on inflow

https://doi.org/10.5194/egusphere-2026-4064
Preprint. Discussion started: 11 September 2026

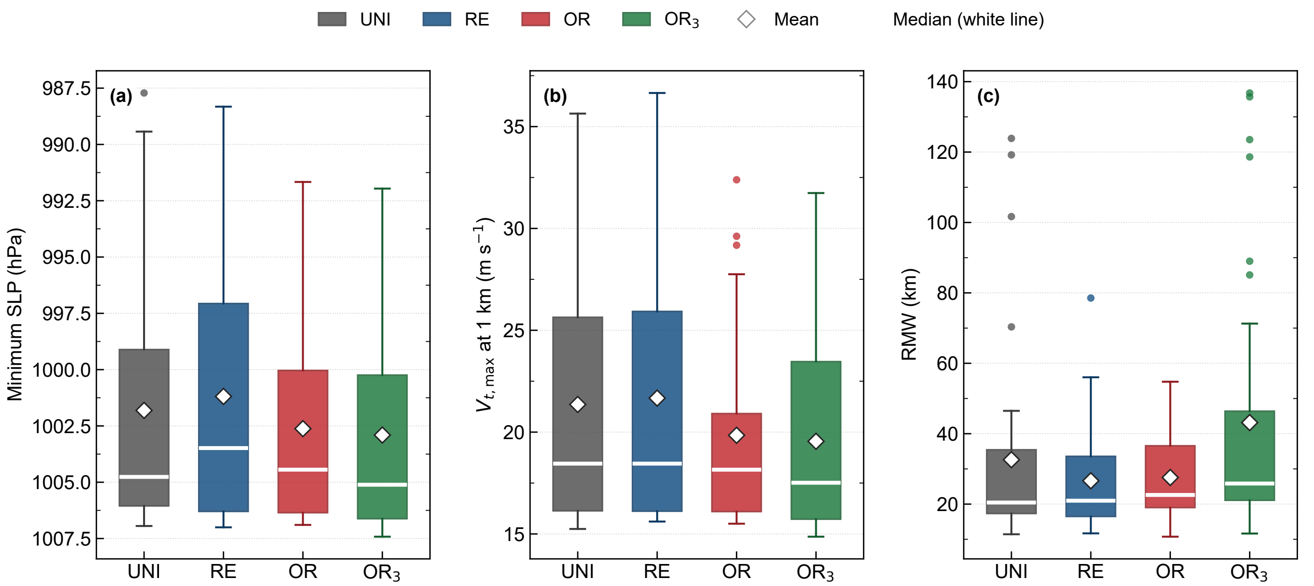

Figure 13. Distributions over 0–36 h of (a) minimum sea-level pressure, (b) peak 1 km tangential wind, and (c) RMW for UNI, RE, OR and OR_3. Diamonds mark means, white lines medians. The RE distributions overlap UNI most closely; OR_3 carries a heavy RMW tail.

alone, and we recommend that adopters of the protocol repeat it as a small ensemble (e.g. by perturbing the initial asymmetry phase) to attach formal confidence intervals to the ranking. Second, the metric integrates over a 36 h window chosen to isolate the adjustment phase; we verified that the *ordering* of the strategies (RE smallest, then OR/OR_3) is preserved when the window is shortened to 12 or 24 h or lengthened to 48 h, the absolute deviations shrinking monotonically as the window lengthens and the storms converge (Fig. 11). The RE advantage is thus an adjustment-phase effect that does not reverse at longer lead times; it simply becomes smaller as all strategies relax toward the benchmark.

Table 1. Mean absolute deviation from the uniform-mesh benchmark (UNI) over 0–36 h, Eq. (7), for the three nest strategies, evaluated from hourly output of each intensity metric. Smaller is better; the smallest value in each row is shown in bold. RE is closest to the benchmark in every metric.

Metric	RE	OR	OR_3
Minimum sea-level pressure (hPa)	**0.72**	0.96	1.08
Maximum 10 m wind $V_{\max}$ ($\mathrm{m\,s^{-1}}$)	**0.65**	1.17	0.91
Peak 1 km tangential wind ($\mathrm{m\,s^{-1}}$)	**0.35**	1.73	1.78
Peak low-level inflow ($\mathrm{m\,s^{-1}}$)	**0.32**	0.36	0.38

https://doi.org/10.5194/egusphere-2026-4064
Preprint. Discussion started: 11 September 2026

5.1 Precipitation structure and the residual nesting error

Finally, simulated radar reflectivity for RE and UNI (Fig. 14) gives the cleanest view of what remains once initialization is fixed. Because the two share an identical initial core, their early reflectivity—the initial convective ring, spiral-band formation, and consolidating eyewall—is essentially indistinguishable, confirming that the modified initialization reproduces not only the benchmark's axisymmetric intensity but also its asymmetric, precipitating structure. As the integration proceeds, small phase differences emerge between RE and UNI in the placement and timing of individual convective features. This is exactly the residual identified in Sect. 5: robust, integrated quantities such as minimum pressure stay close to UNI for a long time, whereas reflectivity—a small-scale, strongly nonlinear field highly sensitive to the boundary-supplied environment (Fig. 15)—amplifies the tiny residual injected by the nesting mechanism and reveals it first, as a phase offset rather than an intensity error. The two diagnostics are therefore complementary: the robust metric demonstrates that the inner-core evolution is faithfully reproduced, and the sensitive field bounds and localizes the small error that nesting—not initialization—unavoidably contributes.

6 Discussion

Three points follow from the comparison. First, *the interpolation step at nest activation, not the fine mesh itself, is the leading-order problem*. All configurations share the same analytic target and the same 2 km inner grid; what separates them is whether the inner core is built natively—in the spirit of direct vortex specification (Kurihara et al., 1993)—or inherited by coarse-to-fine interpolation. Bypassing the interpolation, which is the essence of the RE modification, removes the grid-scale noise and residual imbalance at $t = 0$ (Sect. 3.3) and underlies RE's smooth spin-up and its close tracking of UNI. This echoes, in a nesting context, the long-standing lesson that unbalanced initial increments radiate as inertia–gravity noise and are best avoided at source rather than filtered out afterwards by initialization schemes such as digital filtering (Lynch and Huang, 1992; Daley, 1991; Warner et al., 1997; Harris and Durran, 2010).

Second, *more nesting levels make it worse, not better*. OR_3 passes the inner core through two successive coarse-to-fine interpolations and, far from smoothing the problem away, acquires a systematic wavenumber-4 truncation artefact (Sect. 3.3) and the strongest early adjustment—a transient RMW excursion to $\sim$120 km and a heavy-tailed RMW distribution (Sect. 5). Because a TC's intensification responds precisely to such low-wavenumber, inner-core asymmetries (Montgomery and Kallenbach, 1997; Nolan et al., 2007; Kossin and Schubert, 2001; Persing et al., 2013), adding an intermediate interpolated domain trades diffuse noise for a coherent, dynamically active artefact and delays the organization of the eyewall.

Third, *headline intensity is a weak discriminator; structure and early adjustment are strong ones*. Over 120 h the strategies converge in minimum pressure and peak wind (Fig. 11), which might tempt a modeller to conclude that nest initialization does not matter. The benchmark-referenced, short-window diagnostics show otherwise: the strategies are cleanly separated in initial imbalance, asymmetry spectrum, and the deviation metrics of Table 1, especially in the kinematic fields that feed the secondary circulation. Most tellingly, the initial-core compactness sets the *phase* of the eyewall life cycle: the boundary-layer inflow, the radius–height eyewall structure, the secondary-circulation reorganization, and the RMW/intensity records all show RE leading and OR_3 trailing by a consistent lag (Sects. 4.2–5), so an analysis that samples only a single lead time can mistake

https://doi.org/10.5194/egusphere-2026-4064
Preprint. Discussion started: 11 September 2026

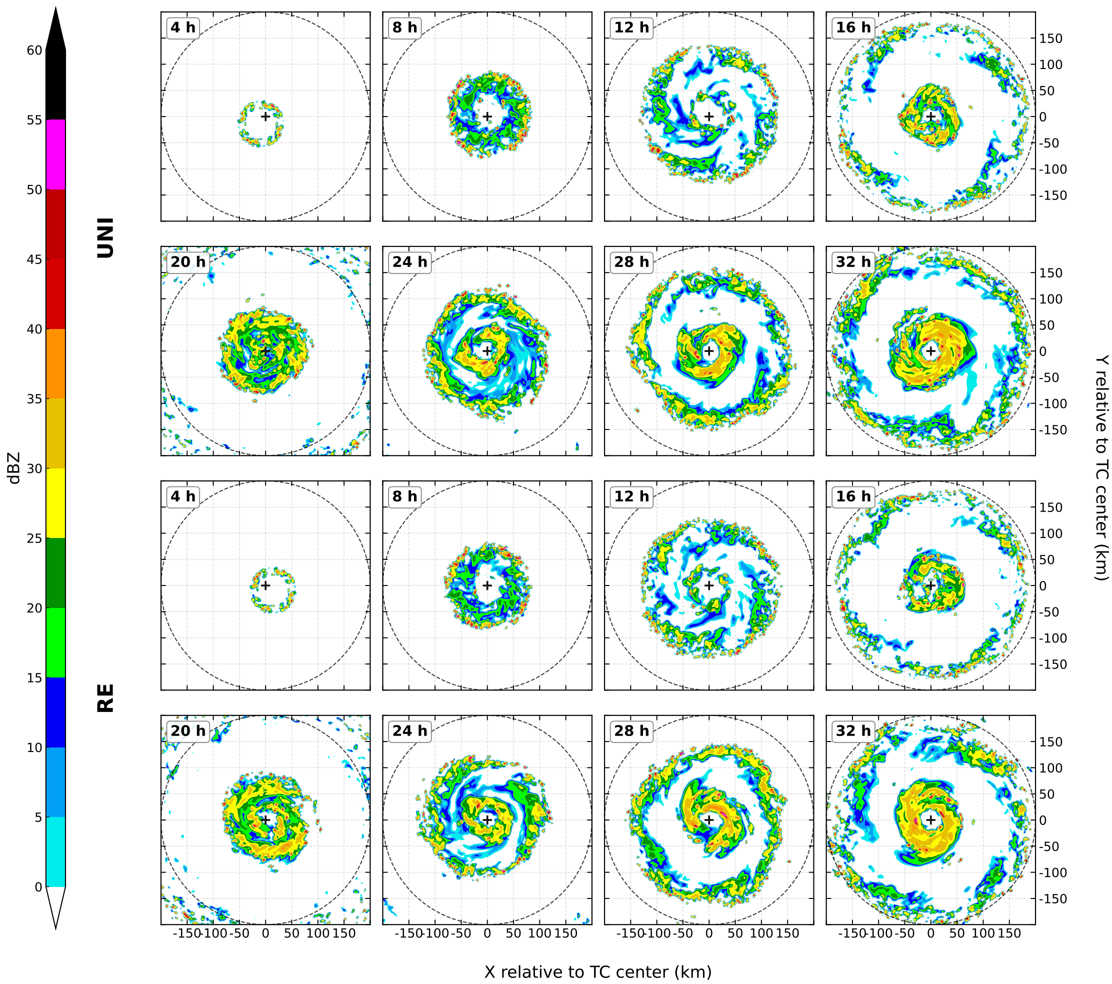

Figure 14. Simulated radar reflectivity (dBZ) for UNI (upper two rows) and RE (lower two rows) at $t = 4$–32h. The two evolve through closely matching convective-ring, spiral-band and eyewall stages.

this timing offset for a structural disagreement—and can even find the runs momentarily coincident (e.g. near $t \approx 96$h) at instants when they merely cross while occupying different points of the same trajectory. For applications that hinge on the first day or two—rapid-intensification onset, inner-core wind structure, storm-surge-relevant wind fields—the difference is operationally meaningful, the more so because rapid-intensification onset is itself sensitive to initial intensity and inner-core size (Li et al., 2022).

The study has clear limits, which also define its intended use. It is idealized—an f-plane vortex in a quiescent environment—and environmental shear, storm motion, and a moving nest would each add processes that this design deliberately excludes in order to isolate the initialization step. The modification changes only how the inner domain is initialized; the standard two-way

https://doi.org/10.5194/egusphere-2026-4064
Preprint. Discussion started: 11 September 2026

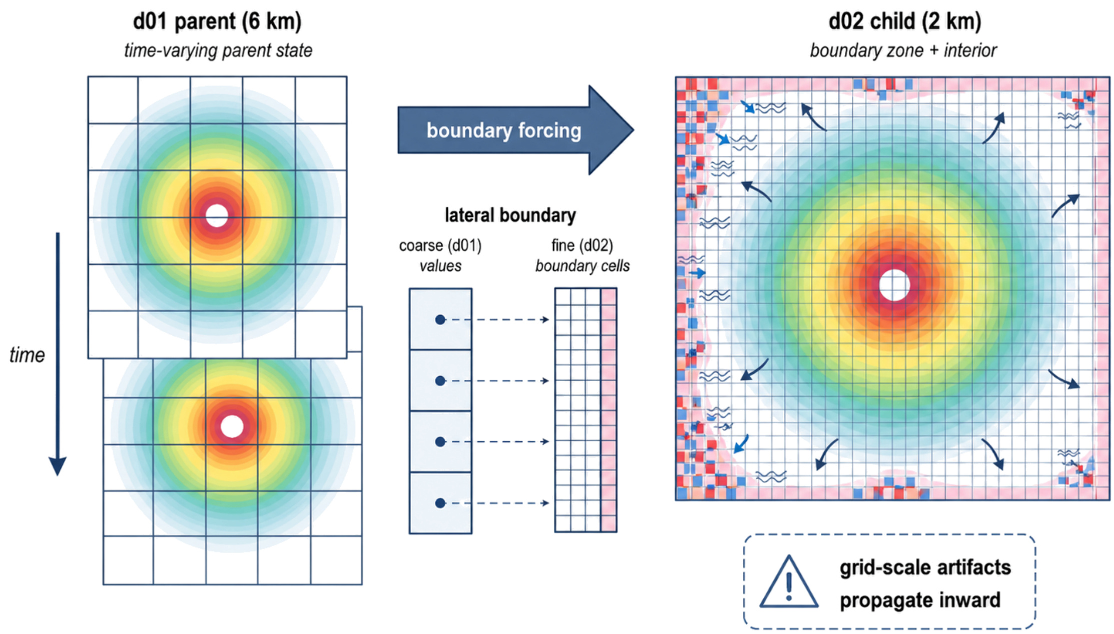

Figure 15. Schematic of the continuous coarse-to-fine boundary forcing during time integration (Step 2), the mechanism responsible for the residual RE–UNI difference. At every child time step the lateral boundaries of the 2 km inner domain (`d02`) are supplied by interpolation from the time-evolving 6 km parent (`d01`); grid-scale mismatches introduced at the interface propagate inward and accumulate over the integration. Because this coupling operates throughout the run—not only at initialization (cf. Fig. 1)—it is the source of nesting error that a native initialization cannot remove, and it surfaces first as a phase (position) offset in the sensitive reflectivity field (Fig. 14) rather than as an intensity error.

coarse-to-fine boundary coupling is retained, and the residual RE–UNI difference (Sect. 5.1) shows that this coupling remains a genuine, if smaller, source of nesting error that a native initialization cannot remove. Because that residual bundles two distinct effects—the coarse-to-fine lateral forcing and the two-way feedback of the child onto the parent—a natural follow-on control is a one-way variant of RE, which would apportion the residual between the two mechanisms (Harris and Durran, 2010). The uniform-mesh reference removes nesting error but not physics error, so the comparison scores *numerical* fidelity to the intended fine-grid solution, not fidelity to nature. None of these limits weakens the central, transferable result: a natively resolved, interpolation-free nest initialization is cheap, is a localized source-code change that leaves the solver untouched, and materially reduces the artefact content of a nested TC simulation.

7 Conclusions

We have presented and documented a modification to the WRF-ARW (v4.5) idealized nesting workflow that initializes the high-resolution inner domain natively—sampling the prescribed analytic vortex directly at its own 2 km resolution rather than

https://doi.org/10.5194/egusphere-2026-4064
Preprint. Discussion started: 11 September 2026

interpolating it from the coarse parent—and have evaluated it against the standard official two-domain (OR) and three-domain (OR_3) configurations and a resolution-matched uniform-mesh benchmark (UNI) whose inner-core initialization is identical to the modified scheme (RE). The main findings are:

1. The standard interpolated initialization injects a grid-scale artefact into the $2\,\mathrm{km}$ inner core—pixelated noise in the two-domain case (OR) and a systematic wavenumber-4 truncation pattern in the three-domain case (OR_3)— together with a small residual radial-wind imbalance near the RMW; the native initialization (RE) removes both (Sect. 3.3).
2. This artefact triggers an early geostrophic-adjustment shock—an inertia–gravity-wave burst, discontinuous early eyewall heating, and in OR_3 a transient RMW excursion to $\sim 120\,\mathrm{km}$ near $t \approx 8$–$12\,\mathrm{h}$—whereas RE spins up smoothly, with the earliest, deepest boundary-layer inflow and the most compact, upright eyewall (Sects. 3.4–4.2).
3. Against the benchmark, RE is closest in every intensity and structure metric, with a near-surface tangential-wind deviation ($0.35\,\mathrm{m\,s^{-1}}$) roughly five times smaller than the interpolated configurations and the smallest minimum-pressure deviation ($0.72\,\mathrm{hPa}$; Table 1).
4. Because RE and UNI share an initial state, their residual difference isolates the error of the nesting mechanism itself; it stays negligible in robust integrated metrics and appears first as a phase offset in the sensitive reflectivity field (Sect. 5.1).

We recommend that idealized nested TC studies initialize the high-resolution nest natively whenever the target vortex is analytically prescribed, and we provide the source modification, namelists, and diagnostic suite as a reusable improvement and a lightweight regression test. Natural extensions include sheared and translating environments and moving nests—particularly the rapid-intensification regime in shear, where high-resolution nests are decisive (Harris et al., 2020; Hazelton et al., 2020, 2023)—coupling the approach to community physics and infrastructure test beds (Heinzeller et al., 2023), and testing whether comparable initialization artefacts arise in the global storm-resolving models now increasingly used for tropical cyclones (Judt et al., 2021; Baker et al., 2024).

Appendix A: Vortex profile parameters

The inner exponent n in Eq. (1) and the outer decay lengths X_1, X_2 and weight A in Eq. (2) are chosen following the observationally constrained relations of Willoughby et al. (2006) so that V, $\mathrm{d}V/\mathrm{d}r$ and the profile are continuous across the transition zone $R_1 \le r \le R_2$. With $V_{\max} = 20\,\mathrm{m\,s^{-1}}$ and $R_{\max} = 40\,\mathrm{km}$ this yields the profile of Fig. 2a and the vorticity of Eq. (3) with maximum $\zeta_{\max} = 14.1 \times 10^{-4}\,\mathrm{s^{-1}}$ at $r = 31.8\,\mathrm{km}$ (Fig. 2b). The wind is tapered smoothly to zero beyond $r_{\mathrm{taper}} = 600\,\mathrm{km}$. The three-dimensional balanced mass field is obtained by the iterative gradient-wind/hydrostatic procedure of Reed and Jablonowski (2011).

https://doi.org/10.5194/egusphere-2026-4064
Preprint. Discussion started: 11 September 2026

Appendix B: Domain-wise idealized initialization

To ensure that each nested domain is initialized from its own analytic solution rather than from parent-domain interpolation, the WRF idealized initialization workflow was modified to write one `wrfinput` file per domain (Fig. B1). In `ideal_em.F`, the initialization procedure was extended from the default single-domain output to a loop over `domain_id = 1, ..., max_dom`. For each domain the corresponding grid is allocated, the namelist configuration is read, the model clock is set, and the idealized initialization routine is called independently.

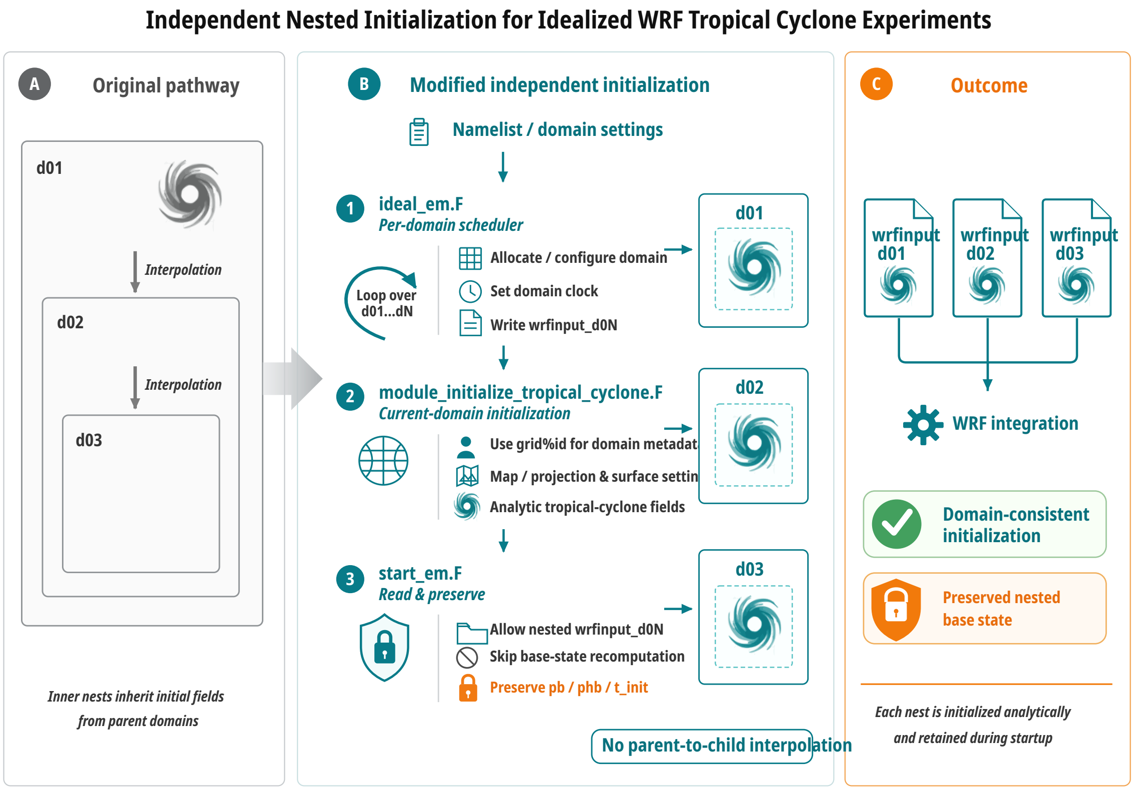

Figure B1. Program framework for domain-wise idealized initialization. The modified workflow replaces parent-to-child interpolation with independent per-domain analytic initialization, while preserving the nested-domain base state during model startup.

The tropical-cyclone initialization metadata in `module_initialize_tropical_cyclone.F`—land-surface type, map projection, and domain-center coordinates—were assigned to the current `grid%id` rather than being fixed to `d01`, so that each nested domain carries metadata consistent with its own grid geometry.

During model startup, `start_em.F` was further modified to let idealized nested domains read their independently generated `wrfinput` files. For child domains initialized from `input_from_file`, recomputation of the base-state fields is skipped so that variables already written by `ideal.exe`—such as `pb`, `alb`, `t_init`, and `phb`—are preserved.

https://doi.org/10.5194/egusphere-2026-4064
Preprint. Discussion started: 11 September 2026

Together these modifications allow the initial conditions of all nested domains to be generated analytically on their own grids, providing a consistent and controllable initialization pathway for idealized multi-nest tropical-cyclone experiments.

Code and data availability. The experimental data used in this study are archived in a Zenodo repository during the review process (Li, 2026) (https://doi.org/10.5281/zenodo.22661292). The modified WRF source files (start_em.F and ideal_em.F), model configuration files, and all automation scripts required to reproduce the figures presented in this paper are also included in the same repository and are publicly accessible at the above URL. These modified source files and scripts are distributed under the MIT License. The original WRF model is in the public domain and is developed by the National Center for Atmospheric Research (NCAR); its license notice is included in the distribution as required by the WRF license terms.

Author contributions. Li designed the study and implemented the native-resolution nest-initialization modification in the WRF-ARW source. Li performed the simulations and the diagnostic analysis and prepared the figures. All authors contributed to interpreting the results and to writing and revising the manuscript.

Competing interests. The authors declare that they have no competing interests.

Disclaimer. Publisher's note: Copernicus Publications remains neutral with regard to jurisdictional claims made in the text, published maps, institutional affiliations, or any other geographical representation in this paper. The authors bear the ultimate responsibility for providing appropriate place names. Views expressed in the text are those of the authors and do not necessarily reflect the views of the publisher.

Acknowledgements. The authors would like to express their sincere gratitude to Professor Yudi Liu for his invaluable guidance and support. This work was jointly supported by the National Natural Science Foundation of China (Grant No. 41875060). The numerical simulations were performed using computational resources provided by the Beijing Parallel Cloud Platform.

Financial support. This work was jointly supported by the National Natural Science Foundation of China (Grant No. 41875060).

https://doi.org/10.5194/egusphere-2026-4064
Preprint. Discussion started: 11 September 2026

References

Abarca, S. F. and Montgomery, M. T.: Essential dynamics of secondary eyewall formation, J. Atmos. Sci., 70, 3216–3230, https://doi.org/10.1175/JAS-D-12-0318.1, 2013.

Baker, A. J., Vannière, B., and Vidale, P. L.: On the realism of tropical cyclone intensification in global storm-resolving climate models, Geophys. Res. Lett., 51, e2024GL109 841, https://doi.org/10.1029/2024GL109841, 2024.

Chavas, D. R., Lin, N., and Emanuel, K.: A model for the complete radial structure of the tropical cyclone wind field. Part I: Comparison with observed structure, J. Atmos. Sci., 72, 3647–3662, https://doi.org/10.1175/JAS-D-15-0014.1, 2015.

Daley, R.: Atmospheric Data Analysis, no. 2 in Cambridge Atmospheric and Space Science Series, Cambridge University Press, Cambridge, UK, ISBN 978-0-521-38215-1, 457 pp., 1991.

Davies, H. C.: A lateral boundary formulation for multi-level prediction models, Q. J. R. Meteorol. Soc., 102, 405–418, https://doi.org/10.1002/qj.49710243210, 1976.

Eliassen, A.: Slow thermally or frictionally controlled meridional circulation in a circular vortex, Astrophys. Norv., 5, 19–60, https://ui.adsabs.harvard.edu/abs/1951ApNr....5...19E/abstract, 1951.

Emanuel, K. A.: An air–sea interaction theory for tropical cyclones. Part I: Steady-state maintenance, J. Atmos. Sci., 43, 585–605, https://doi.org/10.1175/1520-0469(1986)043<0585:AASITF>2.0.CO;2, 1986.

Fierro, A. O., Rogers, R. F., Marks, F. D., and Nolan, D. S.: The impact of horizontal grid spacing on the microphysical and kinematic structures of strong tropical cyclones simulated with the WRF-ARW model, Mon. Weather Rev., 137, 3717–3743, https://doi.org/10.1175/2009MWR2946.1, 2009.

Gentry, M. S. and Lackmann, G. M.: Sensitivity of simulated tropical cyclone structure and intensity to horizontal resolution, Mon. Weather Rev., 138, 688–704, https://doi.org/10.1175/2009MWR2976.1, 2010.

Gopalakrishnan, S. G., Marks, F., Zhang, X., Bao, J.-W., Yeh, K.-S., and Atlas, R.: The experimental HWRF system: A study on the influence of horizontal resolution on the structure and intensity changes in tropical cyclones using an idealized framework, Mon. Weather Rev., 139, 1762–1784, https://doi.org/10.1175/2010MWR3535.1, 2011.

Hack, J. J. and Schubert, W. H.: Nonlinear response of atmospheric vortices to heating by organized cumulus convection, J. Atmos. Sci., 43, 1559–1573, https://doi.org/10.1175/1520-0469(1986)043<1559:NROAVT>2.0.CO;2, 1986.

Harris, L., Zhou, L., Lin, S.-J., Chen, J.-H., Chen, X., Gao, K., Morin, M. J., Rees, S. L., Sun, Y., Tong, M., Xiang, B., Bender, M. A., Benson, R., Cheng, K.-Y., Clark, S. K., Elbert, O., Hazelton, A., Huff, J. J., Kaltenbaugh, A., Liang, Z., Marchok, T., Shin, H. H., and Stern, W. F.: GFDL SHiELD: A unified system for weather-to-seasonal prediction, J. Adv. Model. Earth Syst., 12, e2020MS002 223, https://doi.org/10.1029/2020MS002223, 2020.

Harris, L. M. and Durran, D. R.: An idealized comparison of one-way and two-way grid nesting, Mon. Weather Rev., 138, 2174–2187, https://doi.org/10.1175/2010MWR3080.1, 2010.

Harris, L. M. and Lin, S.-J.: A two-way nested global-regional dynamical core on the cubed-sphere grid, Mon. Weather Rev., 141, 283–306, https://doi.org/10.1175/MWR-D-11-00201.1, 2013.

Hazelton, A., Zhang, X., Gopalakrishnan, S., Ramstrom, W., Marks, F., and Zhang, J. A.: High-resolution ensemble HFV3 forecasts of Hurricane Michael (2018): Rapid intensification in shear, Mon. Weather Rev., 148, 2009–2032, https://doi.org/10.1175/MWR-D-19-0275.1, 2020.

https://doi.org/10.5194/egusphere-2026-4064
Preprint. Discussion started: 11 September 2026

Hazelton, A., Alaka, Jr., G. J., Gramer, L., Ramstrom, W., Ditchek, S., Chen, X., Liu, B., Zhang, Z., Zhu, L., Wang, W., Thomas, B., Shin, J., Wang, C.-K., Kim, H.-S., Zhang, X., Mehra, A., Marks, F., and Gopalakrishnan, S.: 2022 real-time hurricane forecasts from an experimental version of the Hurricane Analysis and Forecast System (HAFSV0.3S), Front. Earth Sci., 11, 1264 969, https://doi.org/10.3389/feart.2023.1264969, 2023.

Heinzeller, D., Bernardet, L., Firl, G., Zhang, M., Sun, X., and Ek, M.: The Common Community Physics Package (CCPP) Framework v6, Geosci. Model Dev., 16, 2235–2259, https://doi.org/10.5194/gmd-16-2235-2023, 2023.

Janjić, Z. I.: The step-mountain eta coordinate model: Further developments of the convection, viscous sublayer, and turbulence closure schemes, Mon. Weather Rev., 122, 927–945, https://doi.org/10.1175/1520-0493(1994)122<0927:TSMECM>2.0.CO;2, 1994.

Judt, F., Klocke, D., Rios-Berrios, R., Vannière, B., Ziemen, F., Auger, L., Biercamp, J., Bretherton, C., Chen, X., Düben, P., Hohenegger, C., Khairoutdinov, M., Kodama, C., Kornblueh, L., Lin, S.-J., Nakano, M., Neumann, P., Putman, W., Röber, N., Roberts, M., Satoh, M., Shibuya, R., Stevens, B., Vidale, P. L., Wedi, N., and Zhou, L.: Tropical cyclones in global storm-resolving models, J. Meteorol. Soc. Jpn., 99, 579–602, https://doi.org/10.2151/jmsj.2021-029, 2021.

Kepert, J. D.: The dynamics of boundary layer jets within the tropical cyclone core. Part I: Linear theory, J. Atmos. Sci., 58, 2469–2484, https://doi.org/10.1175/1520-0469(2001)058<2469:TDOBLJ>2.0.CO;2, 2001.

Kepert, J. D.: How does the boundary layer contribute to eyewall replacement cycles in axisymmetric tropical cyclones?, J. Atmos. Sci., 70, 2808–2830, https://doi.org/10.1175/JAS-D-13-046.1, 2013.

Klemp, J. B., Skamarock, W. C., and Dudhia, J.: Conservative split-explicit time integration methods for the compressible nonhydrostatic equations, Mon. Weather Rev., 135, 2897–2913, https://doi.org/10.1175/MWR3440.1, 2007.

Kossin, J. P. and Schubert, W. H.: Mesovortices, polygonal flow patterns, and rapid pressure falls in hurricane-like vortices, J. Atmos. Sci., 58, 2196–2209, https://doi.org/10.1175/1520-0469(2001)058<2196:MPFPAR>2.0.CO;2, 2001.

Kurihara, Y., Bender, M. A., and Ross, R. J.: An initialization scheme of hurricane models by vortex specification, Mon. Weather Rev., 121, 2030–2045, https://doi.org/10.1175/1520-0493(1993)121<2030:AISOHM>2.0.CO;2, 1993.

Li, X.: Interpolation-free native nest initialization for WRF tropical cyclone simulations, Zenodo Dataset, https://doi.org/10.5281/zenodo.22661292, 2026.

Li, Y., Tang, Y., Toumi, R., and Wang, S.: Revisiting the definition of rapid intensification of tropical cyclones by clustering the initial intensity and inner-core size, J. Geophys. Res. Atmos., 127, e2022JD036 870, https://doi.org/10.1029/2022JD036870, 2022.

Lynch, P. and Huang, X.-Y.: Initialization of the HIRLAM model using a digital filter, Mon. Weather Rev., 120, 1019–1034, https://doi.org/10.1175/1520-0493(1992)120<1019:IOTHMU>2.0.CO;2, 1992.

McWilliams, J. C., Graves, L. P., and Montgomery, M. T.: A formal theory for vortex Rossby waves and vortex evolution, Geophys. Astrophys. Fluid Dyn., 97, 275–309, https://doi.org/10.1080/0309192031000108698, 2003.

Melander, M. V., McWilliams, J. C., and Zabusky, N. J.: Axisymmetrization and vorticity-gradient intensification of an isolated two-dimensional vortex through filamentation, J. Fluid Mech., 178, 137–159, https://doi.org/10.1017/S0022112087001150, 1987.

Montgomery, M. T. and Kallenbach, R. J.: A theory for vortex Rossby-waves and its application to spiral bands and intensity changes in hurricanes, Q. J. R. Meteorol. Soc., 123, 435–465, https://doi.org/10.1002/qj.49712353810, 1997.

Nolan, D. S., Moon, Y., and Stern, D. P.: Tropical cyclone intensification from asymmetric convection: Energetics and efficiency, J. Atmos. Sci., 64, 3377–3405, https://doi.org/10.1175/JAS3988.1, 2007.

Persing, J., Montgomery, M. T., McWilliams, J. C., and Smith, R. K.: Asymmetric and axisymmetric dynamics of tropical cyclones, Atmos. Chem. Phys., 13, 12 299–12 341, https://doi.org/10.5194/acp-13-12299-2013, 2013.

https://doi.org/10.5194/egusphere-2026-4064
Preprint. Discussion started: 11 September 2026

Reasor, P. D., Montgomery, M. T., and Grasso, L. D.: A new look at the problem of tropical cyclones in vertical shear flow: Vortex resiliency, J. Atmos. Sci., 61, 3–22, https://doi.org/10.1175/1520-0469(2004)061<0003:ANLATP>2.0.CO;2, 2004.

Reed, K. A. and Jablonowski, C.: An analytic vortex initialization technique for idealized tropical cyclone studies in AGCMs, Mon. Weather Rev., 139, 689–710, https://doi.org/10.1175/2010MWR3488.1, 2011.

Reed, K. A. and Jablonowski, C.: Idealized tropical cyclone simulations of intermediate complexity: A test case for AGCMs, J. Adv. Model. Earth Syst., 4, M04 001, https://doi.org/10.1029/2011MS000099, 2012.

Rotunno, R. and Emanuel, K. A.: An air–sea interaction theory for tropical cyclones. Part II: Evolutionary study using a nonhydrostatic axisymmetric numerical model, J. Atmos. Sci., 44, 542–561, https://doi.org/10.1175/1520-0469(1987)044<0542:AAITFT>2.0.CO;2, 1987.

Rozoff, C. M., Nolan, D. S., Kossin, J. P., Zhang, F., and Fang, J.: The roles of an expanding wind field and inertial stability in tropical cyclone secondary eyewall formation, J. Atmos. Sci., 69, 2621–2643, https://doi.org/10.1175/JAS-D-11-0326.1, 2012.

Schubert, W. H. and Hack, J. J.: Inertial stability and tropical cyclone development, J. Atmos. Sci., 39, 1687–1697, https://doi.org/10.1175/1520-0469(1982)039<1687:ISATCD>2.0.CO;2, 1982.

Schubert, W. H., Montgomery, M. T., Taft, R. K., Guinn, T. A., Fulton, S. R., Kossin, J. P., and Edwards, J. P.: Polygonal eyewalls, asymmetric eye contraction, and potential vorticity mixing in hurricanes, J. Atmos. Sci., 56, 1197–1223, https://doi.org/10.1175/1520-0469(1999)056<1197:PEAECA>2.0.CO;2, 1999.

Shapiro, L. J. and Willoughby, H. E.: The response of balanced hurricanes to local sources of heat and momentum, J. Atmos. Sci., 39, 378–394, https://doi.org/10.1175/1520-0469(1982)039<0378:TROBHT>2.0.CO;2, 1982.

Sitkowski, M., Kossin, J. P., and Rozoff, C. M.: Intensity and structure changes during hurricane eyewall replacement cycles, Mon. Weather Rev., 139, 3829–3847, https://doi.org/10.1175/MWR-D-11-00034.1, 2011.

Skamarock, W. C. and Klemp, J. B.: A time-split nonhydrostatic atmospheric model for weather research and forecasting applications, J. Comput. Phys., 227, 3465–3485, https://doi.org/10.1016/j.jcp.2007.01.037, 2008.

Skamarock, W. C., Klemp, J. B., Dudhia, J., Gill, D. O., Liu, Z., Berner, J., Wang, W., Powers, J. G., Duda, M. G., Barker, D. M., and Huang, X.-Y.: A description of the Advanced Research WRF model version 4, NCAR Technical Note NCAR/TN-556+STR, National Center for Atmospheric Research, Boulder, CO, USA, https://doi.org/10.5065/1dfh-6p97, 145 pp., 2019.

Smith, R. K., Montgomery, M. T., and Van Sang, N.: Tropical cyclone spin-up revisited, Q. J. R. Meteorol. Soc., 135, 1321–1335, https://doi.org/10.1002/qj.428, 2009.

Stern, D. P. and Nolan, D. S.: Reexamining the vertical structure of tangential winds in tropical cyclones: Observations and theory, J. Atmos. Sci., 66, 3579–3600, https://doi.org/10.1175/2009JAS2916.1, 2009.

Stern, D. P., Vigh, J. L., Nolan, D. S., and Zhang, F.: Revisiting the relationship between eyewall contraction and intensification, J. Atmos. Sci., 72, 1283–1306, https://doi.org/10.1175/JAS-D-14-0261.1, 2015.

Thompson, G., Field, P. R., Rasmussen, R. M., and Hall, W. D.: Explicit forecasts of winter precipitation using an improved bulk microphysics scheme. Part II: Implementation of a new snow parameterization, Mon. Weather Rev., 136, 5095–5115, https://doi.org/10.1175/2008MWR2387.1, 2008.

Vigh, J. L. and Schubert, W. H.: Rapid development of the tropical cyclone warm core, J. Atmos. Sci., 66, 3335–3350, https://doi.org/10.1175/2009JAS3092.1, 2009.

Warner, T. T., Peterson, R. A., and Treadon, R. E.: A tutorial on lateral boundary conditions as a basic and potentially serious limitation to regional numerical weather prediction, Bull. Am. Meteorol. Soc., 78, 2599–2617, https://doi.org/10.1175/1520-0477(1997)078<2599:ATOLBC>2.0.CO;2, 1997.

https://doi.org/10.5194/egusphere-2026-4064
Preprint. Discussion started: 11 September 2026

Willoughby, H. E., Clos, J. A., and Shoreibah, M. G.: Concentric eye walls, secondary wind maxima, and the evolution of the hurricane vortex, J. Atmos. Sci., 39, 395–411, https://doi.org/10.1175/1520-0469(1982)039<0395:CEWSWM>2.0.CO;2, 1982.

Willoughby, H. E., Darling, R. W. R., and Rahn, M. E.: Parametric representation of the primary hurricane vortex. Part II: A new family of sectionally continuous profiles, Mon. Weather Rev., 134, 1102–1120, https://doi.org/10.1175/MWR3106.1, 2006.

Zängl, G., Reinert, D., Rípodas, P., and Baldauf, M.: The ICON (ICOsahedral Non-hydrostatic) modelling framework of DWD and MPI-M: Description of the non-hydrostatic dynamical core, Q. J. R. Meteorol. Soc., 141, 563–579, https://doi.org/10.1002/qj.2378, 2015.